Global Evaluation of Particulate Organic Carbon Parameterizations and Implications for Atmospheric pCO_2

Author:

Lucas J. GLOEGE

Supervisor:

Dr. Galen MCKINLEY

A thesis submitted in partial fulfillment of

the requirements for the degree of

Master of Science

(Atmospheric and Oceanic Sciences)

at the

University of Wisconsin - Madison

2017

Thesis Declaration and Approval

I, Lucas J. GLOEGE, declare that this thesis titled, "Global Evaluation of Particulate Organic Carbon Parameterizations and Implications for Atmospheric pCO_2" and the work presented in it are my own.

Lucas J. Gloege,   _____   _____

Signature   Date

I hereby approve and recommend for acceptance this work in partial fulfillment of the requirements for the degree of Master of Science:

Galen A. McKinley,   _____   _____

Signature   Date

Daniel J. Vimont,   _____   _____

Signature   Date

Ankur R. Desai,   _____   _____

Signature   Date

Abstract

Global Evaluation of Particulate Organic Carbon Parameterizations and Implications for Atmospheric pCO_2

by Lucas J. GLOEGE

under the supervision of Dr. Galen MCKINLEY

This work is under review for publication in Global Biogeochemical Cycles

The shunt of photosynthetically derived particulate organic carbon (POC) from the euphotic zone and deep remineralization comprises the basic mechanism of the 'biological carbon pump.' POC raining through the 'twilight zone' (euphotic depth to 1 km) and 'midnight zone '(1 km to 4 km) is remineralized back to inorganic form through respiration. Accurately modeling POC flux is critical for understanding the 'biological pump' and its impacts on air-sea CO_2 exchange and, ultimately, long-term ocean carbon sequestration. Yet, commonly used parameterizations have not been tested quantitatively against global datasets using identical modeling frameworks. Here, we use a single one-dimensional physical-biogeochemical modeling framework to assess three common POC flux parameterizations in capturing POC flux observations from moored sediment traps and thorium-234 depletion. The exponential decay, Martin curve, and ballast model are compared to data from 11 biogeochemical provinces distributed across the globe. In each province, the model captures satellite-based estimates of surface primary production within uncertainties. Goodness-of-fit is measured by how well the simulation captures the observations, quantified by bias and the root-mean-squared-error and displayed using 'target diagrams.' Comparisons are presented separately for the twilight zone and midnight zone. We find the ballast hypothesis shows no improvement over a globally or regionally parameterized Martin curve. For all provinces taken together,

Martin's b that best fits the data is [0.70, 0.98]; this finding reduces by at least a factor of 3 previous estimates of potential impacts on atmospheric pCO_2 of uncertainty in POC export to a more modest range [-16 ppm, +12 ppm].

Acknowledgements

I would like to start by thanking my advisor, Dr. Galen McKinley. Galen is a passionate researcher and her dedication to each of her students is admirable. Over the years Galen has become more than an advisor, but a role model as well. I truly mean it when I say 'I could not have asked for a better advisor.' Thank you, Galen.

Thanks must also go to Colleen Mouw and Audrey Ciochetto at University of Rhode Island for their collaboration on this project. Their help is appreciated. Also, Darren Pilcher for initially setting up the model and helping me learn MITgcm.

To my thesis readers, Dr. Ankur Desai and Dr. Dan Vimont. I appreciate you taking time out of your busy schedules to provide feedback on this work.

I would also like to thank all the people in Madison that I am fortunate enough to call my friend. In no special order, this includes: Sean Ridge, Skylar Williams, Maria Madsen, Melissa Breeden, Alex Goldstein, David Loveless, and Zac Handlos. We spent many Thursday evenings decompressing at Buck and Badgers playing trivia and managed to rack up $180 in gift cards, good work everybody.

To the owners and baristas at Indie Coffee, thank you for providing me with an alternative thesis writing workspace. A good portion of this thesis was written at Indie.

Contents

List of Figures

List of Tables

List of Abbreviations

AAE	Average Absolute Error
B	Bias
DIC	Dissolved Inorganic Carbon
EXPORTS	Exports Processes in the Ocean from RemoTe Sensing
GLODAP	GLobal Ocean Data Analysis Project
GPP	Gross Primary Production
ME	Modeling Efficiency
MITgcm	Massachusetts Institute of Technology general circulation model
NCEP	National Center for Environmental Prediction
NPP	Net Primary Production
PAR	Photosynthetically Active Radiation
PIC	Particulate Inorganic Carbon
POC	Particulate Organic Carbon
RI	Reliability Index
RMSD	Root Mean Squared Difference
SeaWIFS	Sea-viewing WIde Field-of-view Sensor
uRMSD	unbiased Root Mean Squared Difference
VGPM	Vertically Generalized Production Model

1 Introduction

1.1 The Ocean DIC Profile

Each year, the ocean uptakes 2.1-3.1 PgC [Le Quéré et al., 2016] from the atmosphere in the form of carbon dioxide (CO_2). CO_2 dissolved in the ocean reacts with water forming dissolved carbon dioxide (CO_2^*): which is the sum of aqueous carbon dioxide CO_2^{aq} and carbonic acid (H_2CO_3). H_2CO_3 is a weak acid that dissociates into bicarbonate ions (HCO_3^-) and carbonate ions (CO_3^{2-}). Collectively, these carbon containing species are referred to as dissolved inorganic carbon (DIC): $DIC = [CO_2^*] + [HCO_3^-] + [CO_3^{2-}]$, where the square bracket denotes concentration in seawater per mass ($\mu mol\ kg^{-1}$). The dissociation reactions of H_2CO_3 lowers the ocean's partial pressure of carbon dioxide (pCO_2) allowing the ocean to hold 50 times more carbon compared to the atmosphere [Williams and Follows, 2011].

The vertical distribution of DIC is characterized by biological utilization in the surface and enhancement at depth (Figure 1.1). Two carbon 'pumps' work against this gradient to maintain this profile: the 'physical solubility pump' and the 'biological carbon pump'. Cooler water has the capacity to hold more DIC than warmer water since solubility is inversely proportional to temperature. Cool carbon-laden water is transported to depth via the global overturning circulation. This physical enhancement of DIC at depth is referred to as the physical solubility pump, contributing the majority of the net carbon uptake (Figure 1.1). The biologically driven enhancement of DIC at depth contributes the remaining 10% to the observed DIC

profile. Although the biological pump is small compared to the solubility pump, without it the atmospheric pCO_2 would be 150-200 μatm greater than the current value [Parekh et al., 2006].

Figure 1.1: DIC Profile.
Vertical distribution of dissolved inorganic carbon (DIC). Globally averaged observed vertical profile (solid line) with equilibrium profiles if there were no biological processes and surface water were in complete equilibrium with an atmospheric carbon dioxide for pre-industrial era (long dashes) or 1990 (short dashes). The equilibrium profiles are synonymous with only the the action of the solubility pump while the observed profile is synonymous with the action of the solubility pump plus the biological pump. (Figure courtesy of Williams and Follows [2011])

The oceanic food chain begins with phytoplankton where, through photosynthesis, they synthesize organic matter from DIC and other dissolved nutrients. Only a few of the more than 20,000 phytoplankton species dominate most of the open ocean: small picophytoplankton dominate mid-latitude regions while larger diatoms dominate the high-latitude oceans and tropical upwelling regions. Gross primary production (GPP) is the amount of energy or biomass phytoplankton create in a given amount of time. When cellular respiration (i.e. energy used for growth and development) is subtracted from GPP we are left with net primary production (NPP), which is available to higher trophic levels. Globally, NPP is estimated to be 51 $PgC \ y^{-1}$ to 65 $PgC \ y^{-1}$ [Buitenhuis et al., 2013].

The fate of this organic matter is very complex [Burd et al., 2002], involving interactions of a diverse group of organisms. The large scale sinking of organic matter from the surface ocean is referred to export production, which is affected by both primary productivity [Sarmiento and Gruber, 2006] and the phytoplankton community [Mouw et al., 2016b]. Exported organic matter is respired by heterotrophs, such as zooplankton and bacteria, as it sinks through the water column. This thesis focuses on the biological carbon pump and its parameterization in biogeochemical models.

1.2   The Biological Carbon pumps

The biologically-mediated removal of organic carbon from surface waters against a DIC gradient and its subsequent remineralization at depth is termed the 'biological pump' [Broecker and Peng, 1982; De La Rocha, 2006], which can be separated into

a 'carbonate pump' and a 'soft-tissue pump' [Volk and Hoffert, 1985] as well as a 'microbial pump' [Jiao et al., 2010]. The percentage of net primary production (NPP) exported from the euphotic zone as particulate organic carbon (POC) is at least 5%, with some estimates higher than 40% [Martin et al., 1987; Buesseler, 1998; Schlitzer, 2000; Boyd and Trull, 2007; Buesseler and Boyd, 2009; Henson et al., 2011]. Much of this material is respired primarily by bacteria and zooplankton within the 'twilight zone' (euphotic depth to 1000 m) [Steinberg et al., 2008]; only ~3% of exported NPP reaches the 1000 m depth horizon [De La Rocha and Passow, 2007, and references therin]. On timescales of days to weeks the flux of POC is controlled by sinking speed and degradation rate. If in steady state [Giering et al., 2016], POC flux should be balanced by the input of limiting nutrients to the euphotic zone [Eppley and Peterson, 1979; Passow and Carlson, 2012].

POC flux to depth is the hallmark of the biological pump, and is believed to be critical to setting surface ocean pCO_2 [Parekh et al., 2006; Kwon et al., 2009; Kwon et al., 2011; DeVries et al., 2012]. The pCO_2 gradient across the air-sea interface determines the direction of the carbon flux across the surface. By converting DIC to organic carbon, biological activity reduces surface ocean pCO_2 and promotes CO_2 uptake by the ocean. The downward POC flux then sequesters carbon at depth. Changes in the efficiency of the biological pump has the potential to alter ocean carbon storage and atmospheric CO_2 [Marinov et al., 2008a; Marinov et al., 2008b; Kwon et al., 2009; Henson et al., 2011]. Parekh et al. [2006] estimate the atmospheric pCO_2 would be 150-200 μatm greater than the current value if not for the biological control on the vertical DIC gradient. Kwon et al. [2011] separate the sensitivity of

atmospheric CO_2 to changes in the carbonate pump versus the soft-tissue pump. They find that for a globally-averaged respired carbon increase of 10 $\mu mol \ kg^{-1}$, the carbonate pump increases atmospheric CO_2 by about 3.4% while the soft-tissue pump decreases atmospheric CO_2 by 5.3%, thus there is a net 2% reduction in atmospheric CO_2 when both pumps are accounted for. A schematic of the biological carbon pump is shown in Figure 1.2, which shows the flow of carbon from the atmosphere to the 'twilight zone' (100 - 1000 m) and 'midnight zone' (depths below 1000 m).
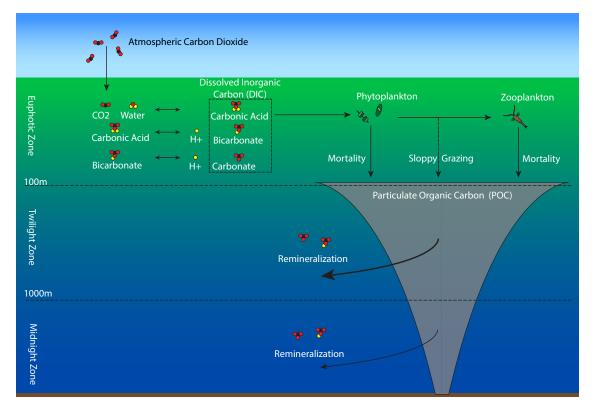

Figure 1.2: Biological Pump Schematic.
This simplified schematic outlines the pathways taken as CO_2 is moved from the atmosphere to the deep ocean.

Projections using earth system models show a sizeable uncertainty across various models with respect to the biological pump's response to 21st century climate change [Bopp et al., 2013; Laufkötter et al., 2015; Hauck et al., 2015; Krumhardt et al., 2016]. Accurate estimation the sensitivity of the biological pump to future climate change is critical to economic evaluations of the impacts of climate change on ecosystem services [Barange et al., 2017]. Parameterizations used in earth system models would ideally capture both the mean POC attenuation and the variability found in available observations, and do so in a mechanistically-realistic manner, in order to reliably predict future change in the strength and efficiency of the biological pump.
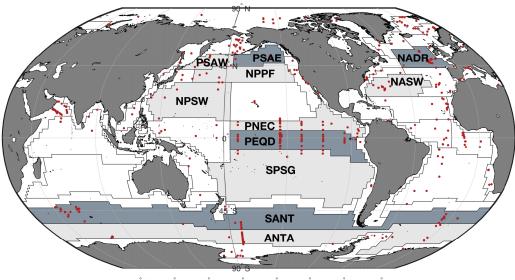
Early parameterizations of POC flux relate export either at a reference depth [Martin et al., 1987] or the euphotic zone primary production [Suess, 1980; Betzer et al., 1984; Pace et al., 1987] to the vertical POC flux through an empirically-derived relationship. Although these parameterizations lack mechanistic realism, the Martin et al. [1987] power law parameterization, in some cases with adjustment to different ocean regions [Henson et al., 2012; Guidi et al., 2015], has been used widely to predict carbon flux below 2000 m [Francois et al., 2002; Honjo et al., 2008]. Alternative to a power law parameterization, an exponential curve has been used to describe attenuation through an empirical fit to observations [Lutz et al., 2002; Boyd and Trull, 2007; Marsay et al., 2015]. Consistent with this approach, first-order kinetics and a constant sinking speed have been used in biogeochemical models, implying exponential decay with depth [Walsh et al., 1988; Banse, 1990; Dutkiewicz et al., 2005; DeVries and Weber, 2017a]. More mechanistic parameterizations, such

as those based on the 'ballast hypothesis' [Armstrong et al., 2002] assume minerals associated with POC increase the POC flux at depth, have been proposed.

To directly compare the various choices available for POC parameterization, a global dataset with consistent treatment and a consistent model framework is required. The choice of seasonal normalization in datasets [Lutz et al., 2002; Lutz et al., 2007; Honjo et al., 2008] can impact statistical fits, and simulated POC fluxes are dependent both on the POC flux parameterization, and also on the simulated surface ocean productivity. In a previous model-data comparison, Howard et al. [2006] used a three-dimensional ocean model in which surface NPP responds to the POC parameterization. They find that the ballast model captures observations more accurately than the Martin curve, and that the geochemical distribution in the deep ocean is sensitive to the parameterization used. However, there has not yet been a comparison across all three common parameterizations in which the modeling framework is identical, including identical surface NPP and POC production to drive the vertical fluxes estimated by each parameterization.

In this study, we compare three common POC flux parameterizations (Table 1.1) using a single one-dimensional numerical modeling framework in which NPP is not responsive to the parameterization used; i.e. each parameterization is driven by the same surface POC source. This model is applied in 11 Longhurst [2006] provinces for which adequate POC flux data are available (Figure 1.3). We quantitatively evaluate the exponential decay model, Martin curve, and the ballast hypothesis using this physical-biogeochemical modeling framework. We use a suite of statistical tests to assess the skill of each POC flux parameterization in capturing

POC flux observations from a global dataset. The global POC flux dataset [Mouw et al., 2016a] consists of POC flux observations from sediment traps supplemented with thorium-234 depletion observations (2% of the data) spanning years 1976 to 2012. We find the parameterization based on the ballast hypothesis shows no improvement over a globally or regionally parameterized Martin curve. This analysis allows commonly used POC flux parameterizations to be evaluated but does not allow for an evaluation of proposed attenuation mechanisms. Finally, the POC flux dataset is used to constrain Martin's b to a global best-fit range [0.70, 0.98] that suggests a far more modest impact on the atmospheric CO_2 concentration than suggested in previous studies [Kwon et al., 2009].

Figure 1.3: Longhurst Provinces.
Simulated provinces presented in the paper are shown in dark gray. Light gray provinces are presented in supplementary. Red dots are locations of flux observations from sediment traps and thorium-234 depletion.

Table 1.1: Three POC flux parameterizations
The parameterization name, POC flux equation, main citation, and studies that incorporate each parameterization are presented in this table. In the equation, $F(z)$ is the POC flux at depth z, w_X is the sinking speed of X = POC, PIC, opal, or dust, $[POC(z)]$ is the volume concentration of labile POC at depth z, $[POC_Y(z)]$ is the volume concentration of POC associated with Y = PIC, opal, or dust at depth z, and b is the attenuation parameter. See section 2.2 - section 2.4 for detailed discussion of each parameterization.

Parameterization	Equation	Citation	Incorporated in
Exponential	$F(z) = w_{poc}[POC(z)]$	Banse [1990]	Dutkiewicz et al. [2005]
Martin curve	$F(z) = F(100)\left(\frac{z}{100}\right)^{-b}$	Martin et al. [1987]	Honjo et al. [2008]
Ballast model	$F(z) = w_{poc}[POC(z)]$ $+ w_{pic}[POC_{pic}(z)]$ $+ w_{opal}[POC_{opal}(z)]$ $+ w_{dust}[POC_{dust}(z)]$	Armstrong et al. [2002]	Moore et al. [2004] Yool et al. [2010] Dunne et al. [2013]

2 Methodology

2.1 Model Description

The Massachusetts Institute of Technology general circulation model (MITgcm) [Marshall et al., 1997a; Marshall et al., 1997b] is configured as a one-dimensional column with 77 vertical layers. Depths increase from a resolution of 10 m in the surface to 650 m in the deepest layer. K-profile parameterization (KPP) simulates vertical mixing [Large et al., 1994]. The model uses a nutrient-restoring scheme with a relaxation time scale of 30 days to approximate advection and diffusive processes that are not directly simulated. Nutrients are restored towards the climatology appropriate for each province in the euphotic zone when the simulated nutrient concentration falls below the climatological value, while nutrients below the euphotic zone are constantly restored towards climatology. Sediments are not included in the model, and thus detritus slowly accumulates in the bottom grid cell; the bottom grid cell is ignored in analyses.

The model is initialized with physical and biogeochemical observations and forced at the surface with monthly climatological meteorological and radiative fields appropriate for each province. Temperature, salinity, and nutrients are prescribed by World Ocean Atlas 2013 [Boyer et al., 2013]. Alkalinity and DIC are prescribed using GLobal Ocean Data Analysis Project (GLODAP) atlas [Key et al., 2004]. Photosynthetically active radiation (PAR) is prescribed using Sea-viewing WIde Field-of-view Sensor (SeaWIFS) data [Frouin, 2002]. Surface dust deposition is provided

by Mahowald et al. [2005]. Surface wind stress is prescribed using National Center for Environmental Prediction (NCEP) reanalysis 1 [Kalnay et al., 1996].

The ecosystem model embedded in MITgcm is that of Dutkiewicz et al. [2005]. The model includes two phytoplankton functional groups (diatoms and small phytoplankton) and one zooplankton class. Phytoplankton growth can be light and nutrient limited. Mortality rate and maximum growth rates of diatoms and small phytoplankton are tuned for each province (Table B.2) to best fit satellite-based estimates of primary productivity (Table B.1). The standard export parameterization for this model is exponential decay, with a remineralization or dissolution rate (k) of 1/10 d^{-1} for POC, 1/150 d^{-1} for biogenic silica (opal), and 1/300 d^{-1} for particulate inorganic carbon (PIC). The sinking speed (w) for POC, PIC, and opal are fixed constants: POC and opal sink at a rate of 10 m d^{-1} while PIC sinks at 15 m d^{-1}. These POC sinking speeds lie within the range of other models: 2.5 m d^{-1} [Yool et al., 2010], 8 m d^{-1} [Dutkiewicz et al., 2005], and 11-85 m d^{-1} [DeVries and Weber, 2017a]. The POC remineralization rate and sinking speed used here imply a remineralization length scale of 100 m, similar to the Lima et al. [2014] value of 130 m and within the range assumed by Moore et al. [2004]. This remineralization length scale is within the 50-200 m range that Mouw et al. [2016b] found for most provinces, and the 69-265 m range derived from the optimization of DeVries and Weber [2017a].

In the model, 7% of phytoplankton are calcifiers, and therefore produce PIC. Production of POC, PIC, and opal are due to mortality of phytoplankton and zooplankton, as well zooplankton grazing on phytoplankton. The tendency of POC,

PIC, and opal production are shown below:

$$\frac{d[X^{prod}(z)]}{dt} = P_X^{prod}(z) + Z_X^{prod}(z) \tag{2.1}$$

where X=POC, PIC, or opal. $P_X^{prod}(z)$ represents production of X ($mgX\ m^{-2}\ d^{-1}$) at depth (z, m) by phytoplankton (P), and $Z_X^{prod}(z)$ represents production of X ($mgX\ m^{-2}\ d^{-1}$) at depth (z, m) by zooplankton (Z).

A 10-year simulation is run after a 10-year model spin up. The model uses a time step of 200 seconds with an 8-day averaging period. This averaging period is chosen to coincide with the time step of the Vertically Generalized Production Model (VGPM) [Behrenfeld and Falkowski, 1997], which is used for comparison to modeled NPP. VGPM satellite-based NPP estimates are obtained from http://www.science.oregonstate.edu/ocean.productivity/ and the modeled NPP is calculated as the integrated productivity in the euphotic zone.

2.2   Exponential Decay Model

The exponential decay model assumes that all the POC is labile with a constant sinking speed, expressed in Equation 2.2 [Banse, 1990].

$$F(z) = w_{poc}[POC(z)] \tag{2.2}$$

where $F(z)$ is the POC flux ($mgC\ m^{-2}\ d^{-1}$) at depth (z, m), w_{poc} is the sinking speed of labile POC ($m\ d^{-1}$), and $[POC(z)]$ is the volume concentration of labile POC

($mgC\ m^{-3}$) at depth. The tendency of POC to sink and remineralize is expressed in the following form:

$$\frac{d[POC(z)]}{dt} = w_{poc}\frac{d[POC(z)]}{dz} - k_{poc}[POC(z)] \tag{2.3}$$

where the first term ($w_{poc}\frac{d[POC(z)]}{dz}$) represents vertically sinking POC into depth level z from above while the second term ($k_{poc}[POC(z)]$) represents a first-order remineralization scheme where POC is instantly remineralized at each depth level (z, m) with k_{poc} being the remineralization rate. An expression for the flux of labile POC is derived by applying Equation 2.2 to a steady state version of Equation 2.3: $F(z) = F(z_o)\exp\left[\frac{(z-z_o)}{\lambda}\right]$, where $F(z_o)$ is the flux at reference depth z_o and λ is the remineralization length scale (e-folding length scale). Table B.3 provides definitions of all equation parameters.

The ecosystem model of Dutkiewicz et al. [2005] treats particulate organic matter as exponentially decaying throughout the water column and assumes all POC is labile. The full tendency of POC is defined in Equation 2.4:

$$\frac{d[POC(z)]}{dt} = \frac{d[POC^{prod}(z)]}{dt} + w_{poc}\frac{d[POC(z)]}{dz} - f_T k_{poc}[POC(z)] \tag{2.4}$$

where the first term is the tendency of POC production (Equation 2.1) and the last two terms represent sinking and remineralization (Equation 2.3). Temperature dependence on remineralization rate is taken into account through an Arrhenius function: $f_T = A * \exp\left[T_{AE}(T^{-1} - T_{ref}^{-1})\right]$, where A, T_{AE} , and T_{ref} are constants and T is

the local temperature (Table B.4). POC flux at each level is calculated using Equation 2.2. This framework will be termed the 'exponential decay model' for POC flux.

2.3 Martin Curve

Using data obtained from free-floating sediment traps, Martin et al. [1987] describe POC flux attenuation using a normalized power function of the following form, commonly referred to as the 'Martin curve':

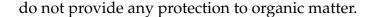$$F(z) = F(100)\left(\frac{z}{100}\right)^{-b} \tag{2.5}$$

where $F(100)$ is the POC flux at 100 m and b is the flux attenuation coefficient. The Martin curve is equivalent to a decreasing remineralization rate with depth or an increasing sinking speed with depth [Lam et al., 2011]. Villa-Alfageme et al. [2016] observed an increase in sinking speed with depth, possibly due to the gradual loss of slow-sinking particles with depth. Small values of b imply a higher transfer efficiency where more carbon remineralizes at deeper depths. Transfer efficiency is defined as the fraction of exported organic matter that reaches a given depth below the depth of export, with 100 m below the depth of export being where transfer efficiency is typically estimated [Buesseler and Boyd, 2009]. Transfer efficiency and b are inversely related: large values of b imply a small transfer efficiency with more carbon remineralizing at shallower depths. Martin et al. [1987] calculated a global

b value of 0.858 using observations from nine locations in the northeast Pacific. Regional variations in the b parameter have been found to improve the statistical fits at the scale of ocean provinces [Henson et al., 2012; Guidi et al., 2015] and across ocean basins [Berelson, 2001; Schlitzer, 2002], implying regional variability in the flux attenuation and transfer efficiency. The spatial pattern of transfer efficiency, and hence b, may be due to ecosystem function, which implies large b values at high latitudes and low b values in the tropics [Henson et al., 2012]. However, Marsay et al. [2015] showed the b parameter correlates with temperature, suggesting a spatial pattern of b that is large in the tropics and small at high latitudes. This pattern is plausibly explained by a slowdown of microbial utilization of carbon as temperature decreases [Pomeroy and Deibel, 1986; Pomeroy and Wiebe, 1991]. Changes in b, when applied globally in a biogeochemical model, may significantly impact atmospheric CO_2 concentrations [Kwon et al., 2009].

In this study, POC fluxes at depth based on the Martin curve are calculated offline from surface production in MITgcm. In keeping with the original intent of the Martin curve, we use Equation 2.5 to calculate the flux at each depth level (z, m) using an export depth of 100 m and export flux, $F(100)$, from the exponential decay model runs. Due to nutrient restoring below the euphotic zone, feedback of shallow remineralization on surface production is negligible; thus, this approach is robust. Runs with both the Martin et al. [1987] global b value of 0.858 as well as the Guidi et al. [2015] and Henson et al. [2012] regional b values are performed for comparison.

2.4   Ballast Hypothesis

The ballast hypothesis proposed by Armstrong et al. [2002] asserts that 'ballast' minerals (PIC, opal, and dust), qualitatively associated with POC, increase the deep ocean POC flux. Using observations from the equatorial Pacific, Armstrong et al. [2002] observed that the ratio of organic carbon flux to total mass flux was nearly constant below 1800 m and concluded ballast minerals are intimately related to the POC flux. Mechanistically, the role of ballast minerals is not entirely clear. It has been proposed that they act to increase the sinking speed and/or protect POC from microbial respiration and zooplankton grazing. Thus, POC that is associated with ballast minerals induces a higher transfer efficiency, delivering more POC to depth. The ballast hypothesis asserts that sinking POC is composed of 'free' and ballast mineral associated fractions (Figure 2.1). The free fraction has a remineralization length scale as labile POC while POC qualitatively associated with ballast minerals is partitioned between a 'soft' and 'hard' subclass, which represent external and internal protection mechanisms, respectively [Armstrong et al., 2002]. External protection constitutes physical removal from hydrolyzing enzymes by adsorption of POC into mineral micropores and increasing sinking speed [Mayer, 1994]; POC associated with the soft fraction has the same remineralization profile as its associated ballast mineral. Internal protection occurs when POC is encased in PIC or opal, sheltering it from degradation until the mineral has dissolved [Armstrong et al., 2002, and references therein]. For this reason, the hard fraction has a very deep remineralization length scale, representing refractory POC. However, Iversen and Robert [2015] concluded that ballast minerals act only to increase sinking speed and
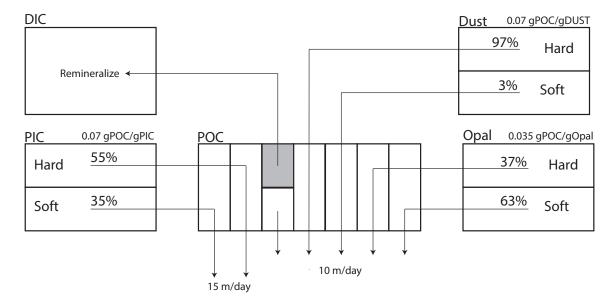
do not provide any protection to organic matter.

Figure 2.1: Ballast Hypothesis Schematic.
Schematic of ballast hypothesis showing particulate organic carbon (PIC), opal, and dust qualitatively associated with particulate organic carbon (POC) with carrying capacities prescribed from Klaas and Archer [2002]. 'Hard' and 'soft' proportions are prescribed according to Lima et al. [2014]. Sinking velocity of PIC is 15 m d^{-1} and 10 m d^{-1} for dust, opal, and labile POC. Remineralized POC enters the DIC pool.

Klaas and Archer [2002] used a global dataset of sediment trap observations in the midnight zone to distinguish three forms of ballast with the following carrying capacities (grams of organic carbon per gram of ballast): PIC (0.094), opal (0.025), and dust (0.035). Additionally, Klaas and Archer [2002] observed 80% of the POC flux to the seafloor was associated with PIC, suggesting it is a more efficient ballast mineral compared to opal and dust. There are three reasons why the carrying capacity of PIC has been suggested to be greater than that of opal and lithogenic dust:

1. PIC sinks ∼50% faster than opal for an equivalent particle radius [Sarmiento and Gruber, 2006], since the density of PIC (2.71 $g\ cm^{-3}$) is ∼30% greater than the density of opal (2.1 $g\ cm^{-3}$) [Klaas and Archer, 2002].

2. Opal production and export is not as spatially uniform as PIC production and export [Sarmiento and Gruber, 2006]. The ratio of opal flux to carbon flux also varies regionally [Ragueneau et al., 2000, Figure 5].

3. Lithogenic fluxes are generally too small to significantly impact the transfer efficiency of organic carbon [Francois et al., 2002].

However, some studies find evidence that does not support PIC having a higher carrying capacity compared to opal or dust [De La Rocha et al., 2008] or show regional variability in the carrying capacity of each ballast mineral [Wilson et al., 2012; Pabortsava et al., 2017].

Published parameterizations for the ballast hypothesis have important differences: Moore et al. [2004] and Armstrong et al. [2002] include PIC, opal, and lithogenic material (dust) as ballast minerals while Yool et al. [2010] and Dunne et al. [2013] omit ballasting from dust. The reader is referred to Moore et al. [2004] and Lima et al. [2014] for a detailed description of the implementation of the ballast hypothesis in a three-dimensional ocean model with dust.

For this study, the ecosystem model of Dutkiewicz et al. [2005] is augmented to include ballasting from PIC, opal, and dust in a manner similar to that of Moore et al. [2004] and Lima et al. [2014]. The implementation of the ballast hypothesis is based on Armstrong et al. [2002] and assumes a portion of the POC production

is associated with PIC and opal production and surface dust deposition. We use carrying coefficients previously used by Moore et al. [2004] and Lima et al. [2014], which are within the observed range of spatial variability [Wilson et al., 2012] and within the range presented in Klaas and Archer [2002] for traps below 2000 m. Flux of POC is calculated by multiplying the sinking speed by the concentration of POC associated with each mineral (Equation 2.6):

$$F(z) = w_{poc}\big[POC(z)\big] + w_{pic}\big[POC_{pic}(z)\big] + w_{opal}\big[POC_{opal}(z)\big] + w_{dust}\big[POC_{dust}(z)\big]$$

(2.6)

where w_x is the sinking speed of X=POC, PIC, opal, or dust, $\big[POC_Y(z)\big]$ is the concentration of POC associated with Y=PIC, opal, or dust, and $\big[POC(z)\big]$ is the concentration of free or labile POC. The tendency of POC associated with ballast mineral Y is separated into a hard and soft subclass (Equation 2.7):

$$\frac{d\big[POC_Y(z)\big]}{dt} = \frac{d\big[POC_Y^{soft}(z)\big]}{dt} + \frac{d\big[POC_Y^{hard}(z)\big]}{dt}$$

(2.7)

POC in the soft subclass decays exponentially with a remineralization rate as its associated ballast mineral while POC in the hard subclass decays exponentially with a very long remineralization rate; POC in each subclass has the same sinking speed as its associated ballast mineral. Each term in $\frac{d\big[POC_{PIC}(z)\big]}{dt}$ is defined in Table B.5 and each term in $\frac{d\big[POC_{opal}(z)\big]}{dt}$ is defined in Table B.6. The source of dust in the model is from surface deposition ($dust^{dep}$, $mgDust\ m^{-2}\ d^{-1}$). POC associated with dust solely occurs in the surface grid cell (Δz_{surf}) and is separated into a

hard and soft subclass which decay exponentially. Each term in the tendency equation for POC associated with dust $\left(\frac{d\left[POC_{dust}(z)\right]}{dt}\right)$ is defined in Table B.7. The tendency of free POC production is calculated by subtracting ballast associated POC from the total POC production: $\frac{d[POC_{free}^{prod}(z)]}{dt} = \frac{d[POC^{prod}(z)]}{dt} - \left[\omega_{PIC}\left(\frac{d\left[PIC^{prod}(z)\right]}{dt}\right) + \omega_{opal}\left(\frac{d\left[opal^{prod}(z)\right]}{dt}\right) + \omega_{dust}\left(\frac{dust^{dep}}{\Delta z_{surf}}\right)\right]$, where $\frac{d\left[X^{prod}(z)\right]}{dt}$ is the production of X=PIC or opal by phytoplankton and zooplankton (Equation 2.1) and ω_Y is the POC carrying capacity for Y=PIC, opal, or dust. Each term in the tendency equation for free POC $\left(\frac{d\left[POC(z)\right]}{dt}\right)$ is defined in Table B.8.

2.5 Analysis

An 8-day climatology of POC flux within each province is created using the Mouw et al. [2016a] data compilation of in situ sediment trap and thorium-234 based measurements. PIC and opal fluxes are not analyzed due to insufficient spatial and temporal resolution in the field data. Dates are converted to day of year and aligned in time using the midpoint of the deployment. POC flux observations within each biogeochemical province, as defined by Longhurst [2006] (provided by VLIZ [2009]), are aggregated and grouped by depth and day of year into 8-day segments. Observations are then aggregated to the model vertical grid in order to quantitatively compare to model output. In order to be considered in our comparison, the following criteria must be met: observations within each province must be available at depths greater than 1000 m, the model must capture the surface ocean production in a manner consistent with satellite retrievals, and provinces must not be coastal.

11 out of 54 provinces met the criteria.

Model performance is assessed by investigating the model-data misfit, defined as $\Delta(i) = \log[M(i)] - \log[O(i)]$ where $M(i)$ and $O(i)$ represent the ith model prediction and i^{th} observed value respectively. Each observation is log base 10 transformed to alleviate skewedness from large values. The water column is partitioned into the twilight zone (100-1000 m) and midnight zone (1000-4000 m), with each analyzed separately. For consideration of variability, the full range of variability for the model and observations across each zone is compared. A set of six summary statistics are used as univariate measures of model performance [Stow et al., 2009]:

$$r = \frac{\sum\limits_{i=1}^{N} \left\{ \log[M(i)] - \overline{\log[M]} \right\} \left\{ \log[O(i)] - \overline{\log[O]} \right\}}{\left\{ \sum\limits_{i=1}^{N} \left\{ \log[M(i)] - \overline{\log[M]} \right\}^2 \sum\limits_{i=1}^{N} \left\{ \log[O(i)] - \overline{\log[O]} \right\}^2 \right\}^{1/2}} \qquad \text{(Correlation)}$$

$$RMSD = \left[\frac{1}{N} \sum\limits_{i=1}^{N} \Delta(i)^2 \right]^{1/2} \qquad \text{(Root Mean Squared Difference)}$$

$$B = \overline{\log[M]} - \overline{\log[O]} \qquad \text{(Bias)}$$

$$AAE = \frac{1}{N} \sum\limits_{i=1}^{N} |\log[M(i)] - \log[O(i)]| \qquad \text{(Average Absolute Error)}$$

$$ME = 1 - \frac{\sum\limits_{i=1}^{N} \{\log[M(i)] - \log[O(i)]\}^2}{\sum\limits_{i=1}^{N} \{\log[O(i)] - \overline{\log[O]}\}^2} = 1 - \left(\frac{RMSD}{s_o} \right)^2 \qquad \text{(Model Efficiency)}$$

$$RI = 10^{RMSD} \qquad \text{(Reliability Index)}$$

The correlation (r) is a measure between -1 and 1 quantifying the degree to which the simulation and observations linearly vary. The correlation only expresses how well the simulation and observations vary together and does not account for systematic biases; a correlation of 1 does not preclude a mean offset between the simulation and observations. Additionally, this value is related to the coefficient of determination (r^2), which expresses the variance explained by a linear regression.

Root mean squared difference ($RMSD$), bias (B), and average absolute error (AAE) are all measures of the discrepancy between the simulated and observed mean. Values near zero imply 'good' model performance and large values imply 'poor' model performance using these metrics. The modeling efficiency (ME) can be used as a transition value between good and poor model performance [Nash and Sutcliffe, 1970]. A skillful model by this metric has an ME value near one. Modeling efficiency is related to $RMSD$: $ME = 1 - \left(\frac{RMSD}{s_o} \right)^2$, where $s_o = \left\{ \frac{1}{N} \sum_{i=1}^{N} \{ \log[O(i)] - \overline{\log[O]} \}^2 \right\}^{1/2}$ is the observed standard deviation. The reliability index (RI) quantifies the average factor by which the model differs from observations. For example, an RI of 2 implies the model predictions need to be multiplied by 2 in order to reconstruct the observations.

Model performance is visualized using normalized 'target diagrams' [Jolliff et al., 2009]. Target diagrams visualize bias and variability together (Figure 3.5), giving them an advantage over the commonly used 'Taylor diagram' [Taylor, 2001], which summarizes only the variability. Normalized target diagrams are based on

the following quadratic relationship:

$$\left(\frac{RMSD}{s_O}\right)^2 = \left(\frac{B}{s_O}\right)^2 + \left(\frac{uRMSD}{s_O}\right)^2 \tag{2.8}$$

where $uRMSD = \left\{\frac{1}{N}\sum_{i=1}^{N}[\Delta(i) - B]^2\right\}^{1/2}$ is the unbiased RMSD (or variance of the model-data misfit) which measures the degree to which the model captures the observed variance, bias (B) is a measure of how well the simulated mean captures the observed mean, and s_o is the observed standard deviation. Target diagrams provide a novel way of visualizing B and $uRMSD$ on a single plot: bias (B) on the y-axis and unbiased RMSD ($uRMSD$) on the x-axis. The radial distance, $\left(\frac{RMSD}{s_o}\right)^2$, is related to the modeling efficiency (ME): $\left(\frac{RMSD}{s_o}\right)^2 = 1 - ME$. ME is negative when the radial distance is greater than one and modeling efficiency is positive when the radial distance is less than one. Therefore, ME is visualized by plotting a circle with a radius of one on a normalized target diagram; skillful models are within the circle. Under- or over-estimation of the variability is quantified by multiplying $uRMSD$ by the sign of the observed standard deviation (s_o) subtracted from the modeled standard deviation (s_M). Equation 2.9 shows the relationship used to construct target diagrams presented in this manuscript, which is equivalent to Equation 2.8:

$$(1 - ME) = B^{*2} + uRMSD^{*2} \tag{2.9}$$

where $B^* = \frac{B}{s_O}$ and $uRMSD^* = \frac{uRMSD}{s_O}sign(s_M - s_O)$. Normalized target diagrams allow the display of multiple models on a single plot. They also visualize how well each model captures the observed mean and variance along with the modeling

efficiency (ME). Target diagrams have previously been used to assess satellite-derived NPP estimates [Friedrichs et al., 2009; Saba et al., 2010; Saba et al., 2011; Lee et al., 2015], surface chlorophyll [Hofmann et al., 2008; Lazzari et al., 2012], and physical variables such as temperature and salinity [Hofmann et al., 2008; Pairaud et al., 2011].

The final component of our analysis is to determine the range of Martin's b that is globally consistent with POC flux observations; and then to use this range to constrain previous estimates of the potential sensitivity of atmospheric pCO_2 to uncertainty in the biological pump [Kwon et al., 2009]. The normalized bias ($B*$), the vertical axis in normalized target diagrams, is our metric for best fit. As discussed in detail in chapter 3, the three parameterizations are better able to capture the observed mean POC flux rather than POC flux variability, motivating the choice of $B*$ as a metric. For this analysis, the model is run for each province with a range of b values from 0.40 to 1.40 (with increments of 0.01), the range of b from Kwon et al. [2009]. $B*$ is calculated using observations only in the midnight zone, and in both the midnight and twilight zones. A particular value of b 'accurately' captures the observed mean if the $B*$ for that model is within the range [-1,1] (Figure 2.2). The best-fit global b range is taken as the interquartile range of all province-specific b values. Atmospheric pCO_2 as a function of b is taken from the global 3-D biogeochemical modeling study of Kwon et al. [2009]. In their most realistic model formulation (i.e. 'nutrient restoring'), biological productivity changed in response to export change and a constant rain ratio (PIC/POC) of 0.08 was used. The full range of pCO_2 reported by Kwon et al. [2009] was based not only on the 0.4-1.4 range

for b, but also on alternate model configurations without PIC export and/or where primary production was fixed even as export changed. These alternate models did provide a much larger pCO_2 range (Table B.9), but are less biogeochemically realistic and theoretically unsound. These models either assume an unrealistic PIC:POC ratio or assume export is independent from nutrient supply; thus we do not use these models in our comparison. For our analysis, their results are digitized and interpolated with a cubic spline [Kwon et al., 2009, their Figure 3c]. The change in atmospheric pCO_2 (referenced to pCO_2 with $b = 0.858$) is then inferred from this curve for the range of b values that we find to best fit POC flux observations.
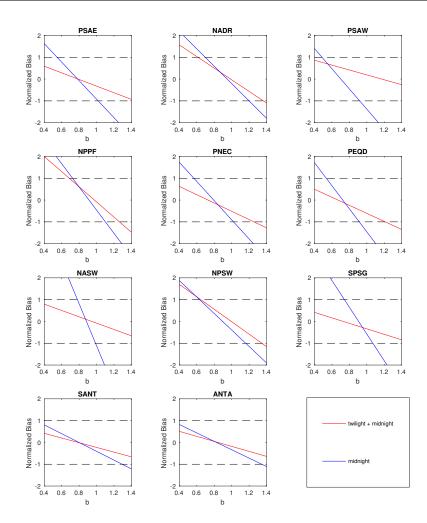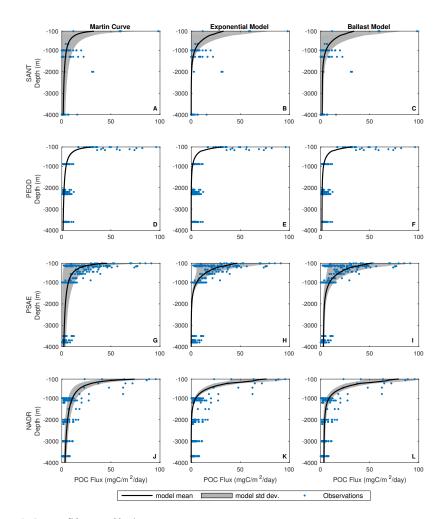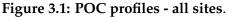
Figure 2.2: $B*$ **Range**.
Normalized bias ($B*$) using a range of b values applied to Equation 2.5. Red line fits Martin curve to twilight and midnight zone observations while the blue curve only fits to observations in the midnight zone.

3 Results

Four biogeochemical provinces out of eleven are selected to be presented in the main text since they span a range of latitudes (Figure 1.3). Simulated POC fluxes for each parameterization in the selected provinces are shown alongside observations in Figure 3.1; all provinces are presented in Figures A.1 - A.14, and considered in the discussion and conclusions. Two provinces, Eastern Pacific subarctic gyres (PSAE) and North Atlantic drift (NADR), were selected for focus because of their expected collocation with the study regions for the Exports Processes in the Ocean from RemoTe Sensing (EXPORTS) field campaign that is presently being planned [Siegel et al., 2016]. These sites also cover a range of ecosystem states. The simulated mean annual primary production in each province captures the climatological range of mean annual primary production, calculated using VGPM (Table B.1). Although the model does not fully capture the observed seasonality across some provinces (Figure 3.2), it does capture the annual primary production, indicating the model is a useful tool to study mean annual export, as done here.

Figure 3.1: POC profiles - all sites.
Simulated POC flux (black) with standard deviation (gray) compared with observed POC flux (blue) for the Martin curve (column 1), exponential model (column 2), and ballast model (column 3) at four provinces (SANT, PEQD, PSAE, NADR). Depth is relative to the surface. Twilight zone extends from 100m - 1000m and midnight zone is >1000m.
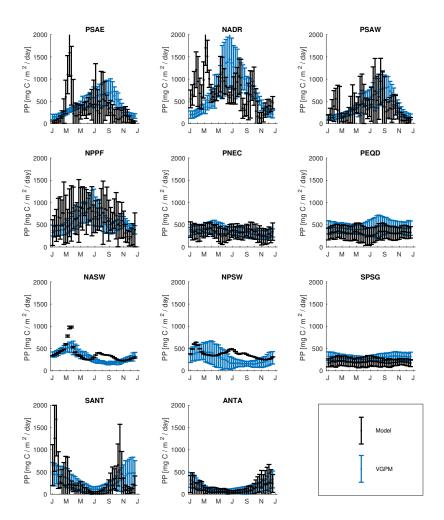
Figure 3.2: Simulated versus Observed Primary Production.
Modeled NPP (black) and satellite based estimate of NPP (blue) at each simulated province.
Error bars represent one standard deviation

3.1 Twilight Zone

For each province, the Martin curve, exponential model, and ballast hypothesis have similar reliability indexes in the twilight zone (Figure 3.3), illustrating that these parameterizations capture observations equally well within the twilight zone. This corroborates Buesseler and Boyd [2009], who show that the Martin curve and exponential model capture observations at shallow depths. The exponential decay model has a tendency to underestimate the flux deep in the twilight zone in some provinces such as the Pacific Equatorial Divergence (PEQD) (Figure 3.4). The exponential model assumes a constant sinking speed and remineralization rate (i.e. constant remineralization length scale) throughout the water column, which often results in fluxes that decrease too quickly with depth [Armstrong et al., 2002; Lutz et al., 2002]. The amount of variability in the modeled flux varies between provinces, much due to variability in primary production.
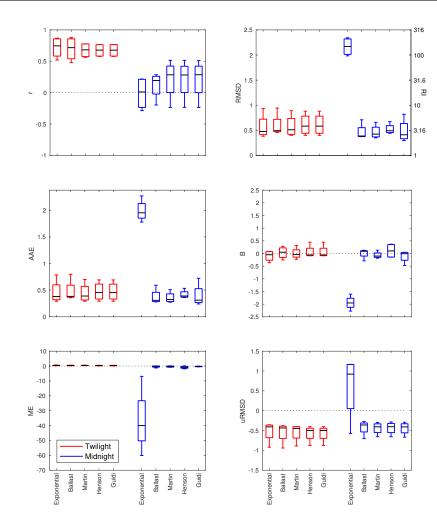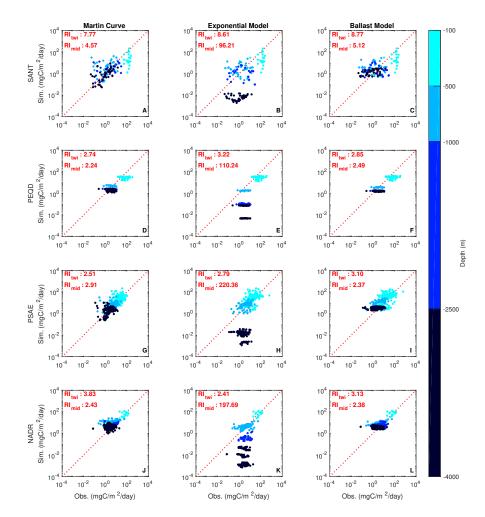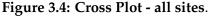
Figure 3.3: Summary Statistics.
Box and whisker plots of summary statistics in the twilight zone (red) and midnight zone (blue) for each parameterization (Exponential, Ballast, Martin et al. [1987] global b value, Henson et al. [2012] regional b values, and Guidi et al. [2015] regional b values). These box and whisker plots account for all simulated provinces (11 total).

Figure 3.4: Cross Plot - all sites.
Cross plot of simulated POC flux versus observed POC flux for the Martin curve, exponential model, and ballast model at four provinces (SANT, PEQD, PSAE, NADR). Colors represent depth below surface: the upper twilight zone (100-500 m), lower twilight zone (500-1000 m), upper midnight zone (1000-2500 m), and lower midnight zone (2500-4000 m). The reliability index (RI) for each zone is indicated at top left in each panel.

The interquartile ranges for the three parameterizations overlap for each of the univariate statistics (Figure 3.3), quantitatively supporting that these parameterizations are equally good at capturing observations in the twilight zone. However, the parameterizations tend to underestimate the observed variability in the twilight zone, evident through negative $uRMSD*$ values (Figure 3.5). Depending on the location, the models either show a slight positive or negative bias (Figure 3.4, Figure 3.5). Overall, all the models perform well in the twilight zone and are more skillful than simply setting the POC flux to be the observed average (Figure 3.5).
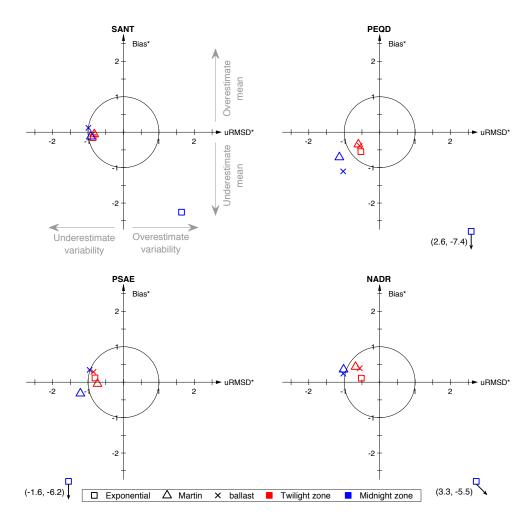
Figure 3.5: Target Diagrams - all sites.
Target diagrams displaying average model skill at each region (SANT, PEQD, PSAE, NADR) for the exponential model, Martin curve, and ballast model in the twilight zone (red) and midnight zone (blue). Outliers are offset in the x and y with the actual position displayed, the small arrow points to the actual position. The black circle is the normalized standard deviation of the observed POC flux. Symbols within the circle indicate that the parameterization captures the observed POC flux more accurately than using the mean of the observed data (Modeling Efficiency (ME) > 0) at each region.

3.2 Midnight Zone

The Martin curve and ballast hypothesis each capture observations well in the midnight zone, while the exponential model underestimates the observed flux at these depths (Figure 3.3; Figure 3.4). The exponential model underestimates the flux at depth since a constant remineralization length scale does not allow for slowdown of remineralization with depth or increasing sinking speed with depth. The global Martin curve slightly underestimates the observed flux in some provinces, such as PEQD (Figure 3.1), resulting from either too low POC fluxes out of the euphotic zone or the use of a b parameter that is too large.

In the midnight zone, the interquartile range for summary statistics overlap for both the Martin curve and ballast hypothesis (Figure 3.3); however, not for the exponential model. Each summary statistic suggests the exponential model performs poorly in the midnight zone compared to the Martin curve and ballast hypothesis:

1. Correlation (r) and interquartile range are nearly symmetric about zero.

2. Large $RMSD$ and AAE compared to Martin curve and ballast hypothesis.

3. Large negative bias (B) compared to Martin curve and ballast hypothesis.

4. Large negative ME, suggesting poor model performance.

The exponential model for the midnight zone generally lies far from the origin in the fourth quadrant in the target diagram (Figure 3.5), consistent with its underestimate of the observed mean and overestimate of variability. However, if only one depth level is resolved in the midnight zone then the normalized target diagram

suggests the exponential model reasonably captures the variability while underestimating the mean (e.g. PSAE). For all provinces, the Martin curve and ballast hypothesis both have a radial distance near unity on the normalized target diagram (Figure 3.5), suggesting these models are equally skillful.

3.3   Regional Attenuation Parameter

Sensitivity of the POC flux to regional Martin curves, using attenuation parameters from Henson et al. [2012] and Guidi et al. [2015], qualitatively agree with each other and with the global b estimates (Figure 3.6, Figure 3.7). Regional b parameters can lead to an improved fit in the midnight zone in specific provinces. For example, the Guidi et al. [2015] regional b parameter reduces the bias in PEQD relative to the Martin et al. [1987] global b value (Figure 3.8). This is further supported by the reliability index (RI) in the midnight zone decreasing from 2.24 using Martin et al. [1987] global b value to 1.97 using the Guidi et al. [2015] regional b parameter (Figure 3.7). However, when all 11 provinces are considered, the interquartile range for each summary statistic overlaps (Figure 3.3), which suggests on a global scale regional b values produce no statistically significant improvement over the Martin et al. [1987] global b value.
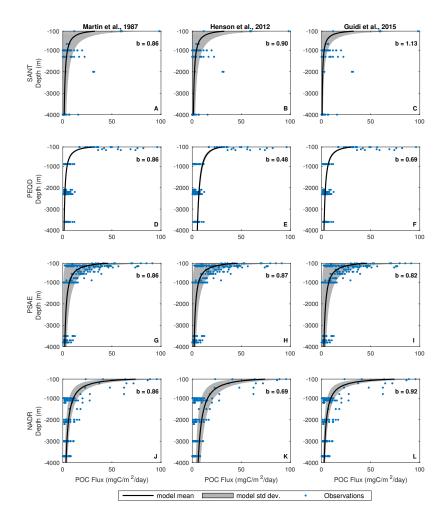
Figure 3.6: POC profiles - regional attenuation.
Simulated POC flux (black) with standard deviation (gray) compared with observed POC flux (blue) using the global b value of Martin et al. [1987] (column 1), regional b value of Henson et al. [2012] (column 2), and regional b values of Guidi et al. [2015] (column 3) at four provinces (SANT, PEQD, PSAE, NADR). Depth is relative to the surface. Twilight zone extends from 100-1000 m and midnight zone is below 1000m.
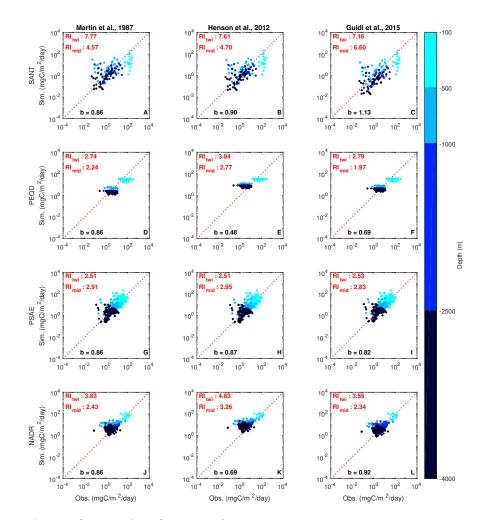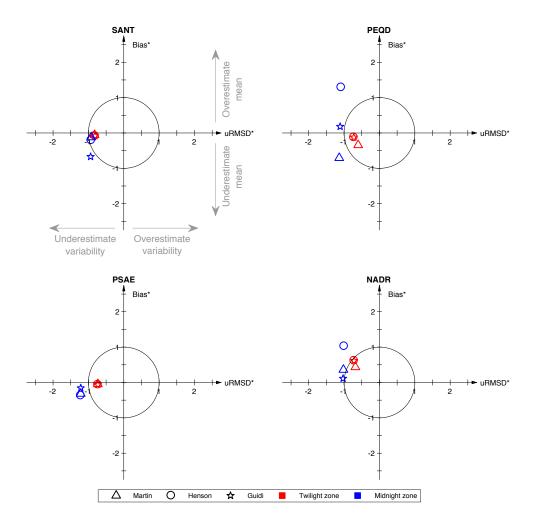
Figure 3.7: Cross plot - regional attenuation.
Cross plot of simulated POC flux versus observed POC flux using the global b value of Martin et al. [1987], Henson et al. [2012] regional b values, and Guidi et al. [2015] regional b values at four provinces (SANT, PEQD, PSAE, NADR). Colors represent depth below surface: the upper twilight zone (100-500 m), lower twilight zone (500-1000 m), upper midnight zone (1000-2500 m), and lower midnight zone (2500-4000 m). The reliability index (RI) for each zone is indicated at top left in each panel.

Figure 3.8: Normalized Target Diagrams - regional attenuation.
Target diagrams displaying average model skill at each region (SANT, PEQD, PSAE, NADR) for the Martin et al. [1987] global b value (Martin), Henson et al. [2012] regional b values (Henson), and Guidi et al. [2015] regional b values (Guidi) in the twilight zone (red) and midnight zone (blue). The black circle is the normalized standard deviation of the observed POC flux. Symbols within the circle indicate that the parameterization captures the observed POC flux more accurately than using the mean of the observed data (modeling efficiency > 0) at each region.

3.4 Constraining Martin's b

Applying $B*$ as a metric to limit Martin's b to a range consistent with the observations in each province (section 2.5) reveals that Martin's global b (=0.858) value is contained within the range of reasonable estimates for each province (Figure 3.9A). When data in the twilight zone and midnight zone are considered, and all provinces b values collected, the interquartile range of b values is 0.68 - 1.13 (Figure 3.9C) while the range is 0.70 - 0.98 when only considering observations solely in the midnight zone (Figure 9D). The midnight zone contains 25-75% of observations in each province (>33% mean, Figure 3.9B) indicating sufficient data are available for the latter comparison.
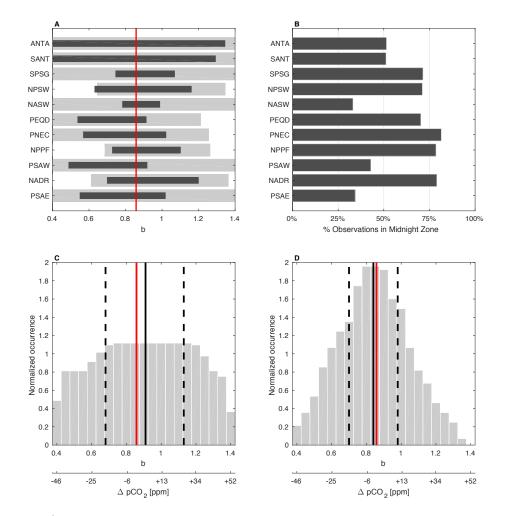
Figure 3.9: Histogram.
A: Range of b values for each province. Light gray bar uses data in the twilight and midnight zone while dark bars only use data in the midnight zone. B: percentage of observations in the midnight zone for each province. C: Histogram of normalized occurrence of b values fit to observations in the twilight and midnight zone D: Histogram of normalized occurrence of b values fit to observations in the twilight and midnight zone. Red line is at Martin et al., 1987 global b value of 0.858. Dotted lines are the 25th percentile and 75th percentile. Solid black line is the median. pCO_2 is relative to pCO_2 with $b = 0.858$ [Kwon et al., 2009].

4 Discussion

We use a consistent modeling framework to compare estimates of vertical POC flux from three common parameterizations to a globally distributed dataset. We find that the Martin curve and the ballast hypothesis capture observations equally well at all depths, which contradicts Howard et al. [2006] who find the ballast hypothesis capture observations more accurately than the Martin curve. Although the carrying capacities in this study differ slightly from Howard et al. [2006] , both studies use coefficients within the range of Klaas and Archer [2002] and within the range of spatial variability [Wilson et al., 2012]. The exponential model is as skillful as the Martin curve and the ballast hypothesis in the twilight zone (100-1000 m), but not as skillful in the midnight zone (1000-4000 m).

Vertical attenuation of POC flux is ultimately controlled by particle sinking speed and remineralization rate, each of which can change as the particle descends through the water column. Potential processes influencing sinking speed and remineralization rate include: mineral ballasting [Armstrong et al., 2002; Francois et al., 2002]., temperature [Laws et al., 2000; Marsay et al., 2015; DeVries and Weber, 2017b], oxygen concentration [Devol and Hartnett, 2001; Van Mooy et al., 2002; Keil et al., 2016; Sanders et al., 2016; DeVries and Weber, 2017b], and particle aggregation [Burd and Jackson, 2009]. Some of these processes have been explicitly parameterized into the 'stochastic, Lagrangian aggregate model of sinking particles (SLAMS)', which was able to reproduce sediment trap observed POC fluxes and some of its regional variation [Jokulsdottir and Archer, 2016]. The relative and global importance of

these processes is unclear [Burd et al., 2016] and their influence on sinking speed is still an active area of research. For example, [Mari et al., 2017] show transparent exopolymer particles (TEP) accumulates in the surface microlayer and needs to be ballasted to overcome its low density and to promote aggregation, which brings into question the classic view that TEP increases POC flux by promoting aggregation through its role as a 'biological glue.' Attenuation of POC flux is also effected by surface processes that modify the character and lability of the POC that is exported. In this context, episodic events [Lebrato et al., 2012; Smith Jr et al., 2014], community structure [Guidi et al., 2009; Guidi et al., 2016], and zooplankton processes [Giering et al., 2014; Cavan et al., 2015; Cavan et al., 2017; Steinberg and Landry, 2017] are all likely important.

We find that this implementation of the ballast hypothesis captures observations in the twilight zone and midnight zone no better than the global and regional Martin curves. This does not invalidate the ballast hypothesis, but instead indicates that the interaction of ballast minerals with POC, as parameterized using standard approaches, is not necessary to model POC flux in a manner that is statistically consistent with observations from water column. A major issue here is, of course, the limited coverage of these data in space and time [Mouw et al., 2016a; Mouw et al., 2016b; Burd et al., 2016; Siegel et al., 2016] . The ballast hypothesis is based on a long-known correlation between the flux of POC and the flux of ballast minerals [Deuser et al., 1981] which has been used to suggest ballast minerals are responsible for the flux of POC at depth, either by increasing the sinking speed or protecting organic matter from oxidation [Armstrong et al., 2002; Francois et al., 2002; Klaas and

Archer, 2002]. The organic matter content of sinking particles in the midnight zone is observed to be approximately 5% by weight [Armstrong et al., 2002]. An alternative view of this correlation is that sinking POC scavenges neutrally-buoyant minerals [Passow, 2004], which has been corroborated with a laboratory study [Passow and De La Rocha, 2006]. Additionally, Passow and De La Rocha [2006] observed the POC to dry weight percent concentration to be 2-3%, which is similar to the 5% observed by Armstrong et al. [2002] in deep sediment traps, suggesting this may be the carrying capacity of suspended minerals for POC. Many studies support the claim that ballast minerals increase the sinking speed of aggregates [De La Rocha and Passow, 2007; Ploug et al., 2008; Iversen and Ploug, 2010]. However, the literature provides both supporting [Arnarson and Keil, 2005; Engel et al., 2009; Le Moigne et al., 2013] and opposing [Ingalls et al., 2006; Ploug et al., 2008; Iversen and Robert, 2015] mechanistic evidence with respect to the degree to which ballast minerals protect organic matter from oxidation.

4.1 Modeling Recommendations

Each parameterization investigated in this study may be useful in modeling studies, but should be selected with consideration of the time and depth scales of interest. All three parameterizations capture mean observations within the twilight zone and therefore would be suitable for studies investigating the surface ocean on annual to decadal time scales, i.e. where accurately capturing the deep ocean is not crucial. However, for studies of the carbon cycle on centennial to millennial time scales, including assessments of long-term ocean carbon sequestration, carbon

supply to the deep ocean should be important. In this case, the Martin curve and the ballast hypothesis capture observations at depth equally well on the mean and therefore would both be suitable.

We find that the empirical Martin curve has a predictive power comparable to the mechanistic ballast hypothesis, despite the fact that it lacks a mechanistic foundation. Though regional variability in the b parameter may improve the realism of the Martin curve [Henson et al., 2012; Guidi et al., 2015], it is still not mechanistic. The exponential decay model's first-order kinetics are mechanistic to a degree, but this approach excludes suggested mechanisms such as increasing sinking speed and remineralization length scale with depth [Villa-Alfageme et al., 2016]. The ballast hypothesis is more mechanistic by allowing for refractory POC and allowing ballast associated POC to sink faster with a longer remineralization length scale. However, sinking speed and remineralization length scale of POC and ballast minerals still do not increase with depth. Even though the ballast hypothesis is more mechanistic than the exponential model and the Martin curve, it does not explain the observed variability in POC flux at depth, which highlights a need for more complete quantification of export mechanisms.

In order to improve simulations of the biological pump, the relative significance of mechanisms driving POC flux attenuation need to be better understood. The primary limitation on this understanding is the lack of observational data with sufficient spatio-temporal resolution to resolve ecosystem processes in the surface ocean that generate POC and at the same time the processes driving remineralization at depth [Buesseler and Boyd, 2009; Siegel et al., 2016; Burd et al., 2016]. Drivers

of temporal variability in these mechanisms need also to be elucidated. To better constrain a model on seasonal timescales, having sediment trap data with higher temporal resolution and more sampling depths would be of great utility.

4.2   Impacts of Uncertainty in the Biological Pump on Atmospheric pCO_2

The biological pump is believed to play an important role regulating atmospheric pCO_2 [Parekh et al., 2006; Kwon et al., 2009] and may help explain the drawdown of atmospheric pCO_2 during glacial periods [Sigman and Boyle, 2000; Buchanan et al., 2016] by sequestering carbon in the deep ocean [Yu et al., 2016]. Carbon raining to the 'midnight zone' (>1000 m) can be considered sequestered because it will be out of contact with the atmosphere for at least 100 years [Primeau, 2005; Ciais, 2014]. Using earth system model experiments, Buchanan et al. [2016] find that the biological pump explains about 58% of the increase in atmospheric pCO_2 from the last glacial maximum to pre-industrial times. The current uncertainty with respect to the biological carbon pump's role in setting atmospheric pCO_2 has significant implications for our understanding of global climate regulation on time frames ranging from centennial to millennial.

Here, we find the best-fit global range for b is 0.68 - 1.13 across both the twilight and midnight zone, and 0.70 - 0.98 for only the midnight zone (section 3.4). These ranges are substantially less than 0.4 to 1.4 used in the model of Kwon et al. [2009] to estimate potential impacts of uncertainty in the biological pump on atmospheric

pCO_2. In their most realistic model configuration, this range of b leads to a range of equilibrium atmospheric pCO_2 of almost 100 ppm [-46ppm, +52ppm]. Since only the carbon that reaches the midnight zone is sequestered on the long-term, our data-constrained range of b that is most applicable to the control of atmospheric pCO_2 is for the midnight zone only, 0.70 - 0.98. This constrained range leads to change in atmospheric pCO_2 of -16 ppm to +12 ppm in the Kwon et al. [2009] model (Table B.9). This indicates that uncertainty in the biological pump, as globally constrained by the available POC flux data, has the potential to vary modern atmospheric pCO_2 by approximately 1/3 the range suggested by Kwon et al. [2009], i.e. only a few tens of ppm [-16 ppm, +12 ppm].

5 Conclusions

5.1 Conclusions

The Mouw et al. [2016a] dataset is a comprehensive collection of POC flux measurements that allows a regional assessment of the skill of the Martin curve, exponential decay model, and ballast hypothesis parameterizations. When these three parameterizations are compared to observations throughout the water column in 11 biogeochemical provinces we find:

1. Twilight zone observations are captured equally well by the all three parameterizations.

2. Midnight zone observations are captured equally well by the Martin curve and ballast hypothesis.

All three parameterizations would be equally good choices for modeling studies addressing the upper ocean, but only the ballast hypothesis or Martin curve should be selected if export to depths below 1000 m is of interest.

Parameterizations using the global b value of Martin et al. [1987] were compared with province specific b values of Guidi et al. [2015] and Henson et al. [2012]. Province-specific b values can reduce the bias in the midnight zone POC fluxes in some regions relative to Martin's global b value (Figure 3.1). However, when all provinces are considered, the interquartile range for each summery statistic overlaps (Figure 3.3), indicating no global benefit of province-specific b values.

Province-specific b values may still be suitable for studies with a regional focus. For all provinces taken together, the range of Martin's b that best fits data from the midnight zone where long-term carbon sequestration occurs is [0.70, 0.98]. Based on previous global biogeochemical modeling [Kwon et al., 2009], this limited range of b has the capacity to change atmospheric pCO_2 by only a few tens of ppm [-16 ppm, +12 ppm]. Though this suggests that atmospheric pCO_2 is not as strongly impacted by uncertainty in the biological carbon pump as previously suggested, the transport of organic matter to depth is most certainly critical to the function of ocean ecosystems. It thus remains critical to improve model representations of these processes.

The paucity of high-resolution observations makes it impossible to discern the relative importance of various export mechanisms, many of which are discussed in chapter 4. At a given depth level, the Mouw et al. [2016a] dataset shows variability spanning an order of magnitude (Figure 3.1) that cannot yet be mechanistically explained, and thus cannot yet be accurately modeled. The role of ecosystem structure on export, the biotic and abiotic transformation of particles to different class sizes, and variability through space and time are key areas of research [Burd et al., 2016; Mouw et al., 2016b]. There is also a great need for seasonally resolved observations at a variety of locations for more complete elucidation and quantification of export mechanisms [Siegel et al., 2016]. Improved mechanistic understanding will directly support the development of next-generation model parameterizations.

5.2 Caveats

This study uses a one dimensional-model forced at the surface with climatology. We use a consistent modeling framework to compare three common POC flux parameterizations to observations. We force the model at the surface with climatological radiative and meteorological fields. Reduced variability in the forcing field inhibits the model's ability to capture POC flux variability associated with physical forcing. The steady state assumption is also used, which neglects the influence of horizontal advection of POC. The model is also sensitive to changes in phytoplankton/zooplankton growth rates, mortality rates, and half saturation rates. This sensitivity made it difficult to accurately capture seasonality observed in satellite-based estimates of primary production, which inhibited our ability to study POC flux on a seasonal level. Sparse sampling (spatially and temporally) force us to compare model output to climatological observations within ocean provinces.

5.3 Future work

The Mouw et al. [2016a] data compilation is a comprehensive collection of POC flux observations. This dataset is invaluable to quantifying and validating mechanisms driving POC export. Future work with this dataset could include: quantifying the degree to which temperature and oxygen capture the observed POC flux, assessing the degree to which parameterized export mechanisms (besides the ballast model) capture observations, and quantifying changes in export.
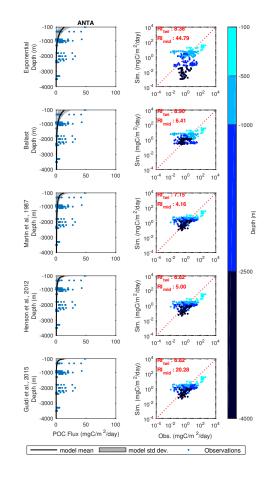
A Supplementary Figures

Figure A.1: ANTA.
Left: Simulated POC flux (black) with standard deviation (gray) compared with observed POC flux (blue) for the exponential model, ballast model, Martin et al. [1987] global b value, Henson et al. [2012] b value, and Guidi et al. [2015] b value at the ANTA province. Right: cross plot of simulated POC flux vs observed POC flux for each model. Color indicates depth.
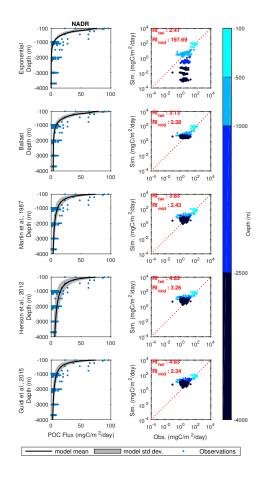
Figure A.2: NADR.
Simulated POC flux (black) with standard deviation (gray) compared with observed POC flux (blue) for the exponential model, ballast model, Martin et al. [1987] global b value, Henson et al. [2012] b value, and Guidi et al. [2015] b value at the NADR province. Right: cross plot of simulated POC flux vs observed POC flux for each model. Color indicates depth.
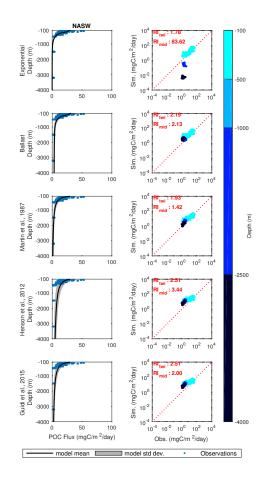
Figure A.3: NASW.
Left: Simulated POC flux (black) with standard deviation (gray) compared with observed POC flux (blue) for the exponential model, ballast model, Martin et al. [1987] global b value, Henson et al. [2012] b value, and Guidi et al. [2015] b value at the NASW province. Right: cross plot of simulated POC flux vs observed POC flux for each model. Color indicates depth.

Figure A.4: NPPF.
Left: Simulated POC flux (black) with standard deviation (gray) compared with observed POC flux (blue) for the exponential model, ballast model, Martin et al. [1987] global b value, Henson et al. [2012] b value, and Guidi et al. [2015] b value at the NPPF province. Right: cross plot of simulated POC flux vs observed POC flux for each model. Color indicates depth.
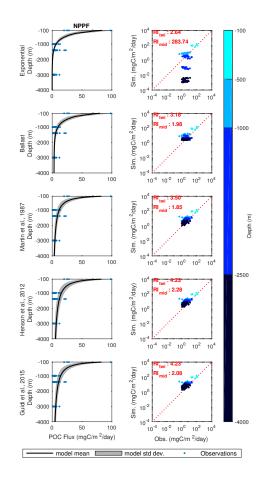
Figure A.5: NPSW.
Left: Simulated POC flux (black) with standard deviation (gray) compared with observed POC flux (blue) for the exponential model, ballast model, Martin et al. [1987] global b value, Henson et al. [2012] b value, and Guidi et al. [2015] b value at the NPSW province. Right: cross plot of simulated POC flux vs observed POC flux for each model. Color indicates depth.
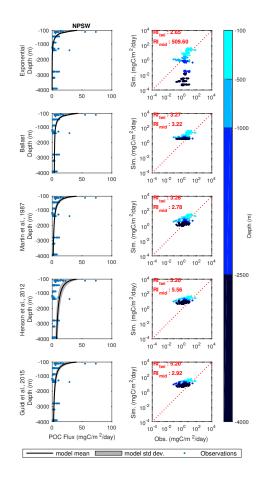
Figure A.6: PEQD.
Left: Simulated POC flux (black) with standard deviation (gray) compared with observed POC flux (blue) for the exponential model, ballast model, Martin et al. [1987] global b value, Henson et al. [2012] b value, and Guidi et al. [2015] b value at the PEQD province. Right: cross plot of simulated POC flux vs observed POC flux for each model. Color indicates depth.
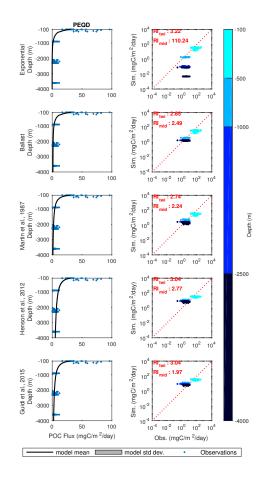
Figure A.7: PNEC.
Left: Simulated POC flux (black) with standard deviation (gray) compared with observed POC flux (blue) for the exponential model, ballast model, Martin et al. [1987] global b value, Henson et al. [2012] b value, and Guidi et al. [2015] b value at the PNEC province. Right: cross plot of simulated POC flux vs observed POC flux for each model. Color indicates depth.

Figure A.8: PSAE.
Left: Simulated POC flux (black) with standard deviation (gray) compared with observed POC flux (blue) for the exponential model, ballast model, Martin et al. [1987] global b value, Henson et al. [2012] b value, and Guidi et al. [2015] b value value at the PSAE province. Right: cross plot of simulated POC flux vs observed POC flux for each model. Color indicates depth.

Figure A.9: PSAW.
Left: Simulated POC flux (black) with standard deviation (gray) compared with observed POC flux (blue) for the exponential model, ballast model, Martin et al. [1987] global b value, Henson et al. [2012] b value, and Guidi et al. [2015] b value at the PSAW province. Right: cross plot of simulated POC flux vs observed POC flux for each model. Color indicates depth.
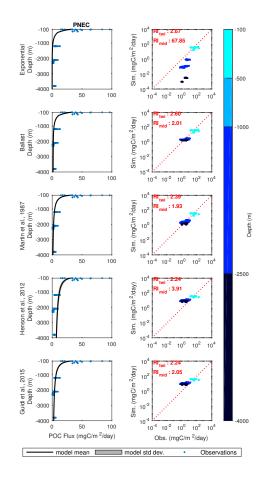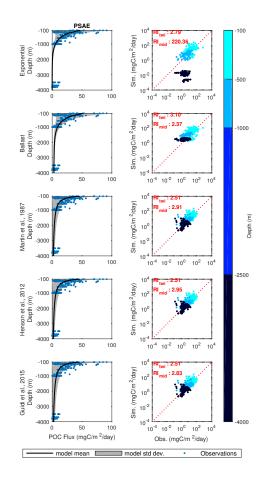
Figure A.10: SANT.
Left: Simulated POC flux (black) with standard deviation (gray) compared with observed POC flux (blue) for the exponential model, ballast model, Martin et al. [1987] global b value, Henson et al. [2012] b value, and Guidi et al. [2015] b value at the SANT province. Right: cross plot of simulated POC flux vs observed POC flux for each model. Color indicates depth.
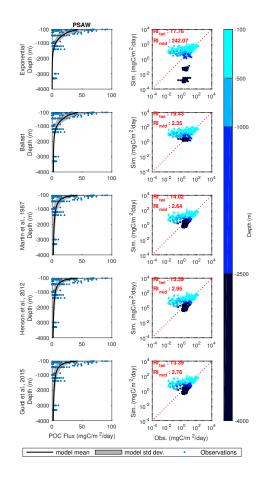
Figure A.11: SPSG.

Left: Simulated POC flux (black) with standard deviation (gray) compared with observed POC flux (blue) for the exponential model, ballast model, Martin et al. [1987] global b value, Henson et al. [2012] b value, and Guidi et al. [2015] b value at the SPSG province. Right: cross plot of simulated POC flux vs observed POC flux for each model. Color indicates depth.
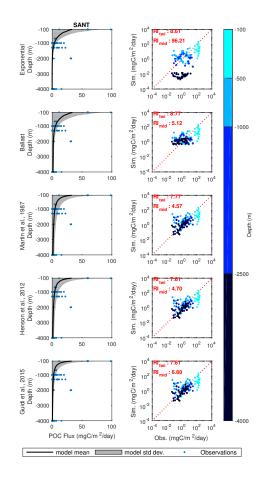
Figure A.12: Target diagrams.
Target diagrams displaying average model skill at each region for the exponential model, Martin curve, and ballast model in the twilight zone (red) and midnight zone (blue). The black circle is the normalized standard deviation of the observed POC flux. Symbols within the circle indicate the parameterization captures the observed POC flux more accurately than using the mean of the observed data (modeling efficiency > 0) at each region.

Figure A.13: Target diagrams - regional b values.
Target diagrams displaying average model skill at each region for the Martin et al. [1987] global b value (Martin), Henson et al. [2012] regional b values (Henson), and Guidi et al. [2015]regional b values (Guidi) in the twilight zone (red) and midnight zone (blue). The black circle is the normalized standard deviation of the observed POC flux. Symbols within the circle indicate the parameterization captures the observed POC flux more accurately than using the mean of the observed data (modeling efficiency > 0) at each region.

Figure A.14: Parameterization RMSD.
RMSD value for each parameterization in the twilight zone (red) and midnight zone (blue). Parameterizations below the black line have a positive modeling efficiency and therefore considered skillful.
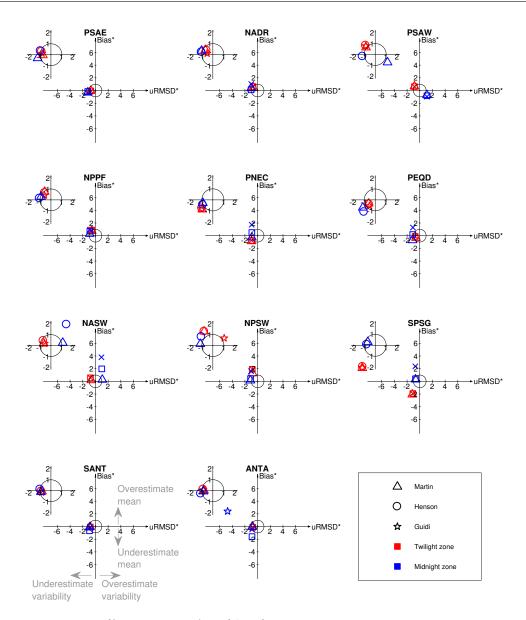
B Supplementary Tables

Table B.1: Annual Primary Production
Annual primary production.

Province [ShortName]	VGPM [gm^{-2}]	Simulation [gm^{-2}]
NPSW	96 ± 53	137 ± 1
PSAW	148 ± 55	113 ± 113
SPSG	108 ± 29	71 ± 34
NADR	251 ± 88	249 ± 100
NASW	113 ± 23	134 ± 2
NPPF	202 ± 61	230 ± 140
PNEC	128 ± 37	118 ± 58
PEQD	155 ± 53	114 ± 58
ANTA	51 ± 31	39 ± 49
SANT	100 ± 59	83 ± 88
PSAE	148 ± 45	108 ± 99

Table B.2: Ecosystem Parameters
Ecosystem parameters in each province. For ecosystem equations, see Dutkiewicz et al. [2005].

Province [ShortName]	Max growth rate (small phyto.) $[day^{-1}]$	Max growth rate (large phyto.) $[day^{-1}]$	Mortality rate (small phto.) $[day^{-1}]$	Mortality rate (large phyto.) $[day^{-1}]$	euphotic depth $[m]$
NPSW	2.6	1.1	15	15	150
PSAW	0.6	1.1	15	15	75
SPSG	3.5	3.5	10	10	150
NADR	0.6	0.6	10	10	75
NASW	1.3	1.1	15	15	150
NPPF	0.6	1.1	15	15	100
PNEC	2.6	2.6	15	15	100
PEQD	2.6	2.6	15	15	100
ANTA	1.3	1.1	15	15	100
SANT	1.3	1.1	15	15	100
PSAE	1.1	0.6	10	10	75

Table B.3: Equation Parameter Definitions
Definition of equation parameters.

Parameter	Units	Definition
$F(z)$	$mgC\ m^{-2}\ d^{-1}$	POC flux
$[POC(z)]$	$mgC\ m^{-3}$	Volume concentration of labile POC
$[POC_Y(z)]$	$mgC\ m^{-3}$	Volume concentration of POC associated with Y
$[POC_Y^{hard}(z)]$	$mgC\ m^{-3}$	Volume concentration of POC associated with Y in hard subclass
$[POC_Y^{soft}(z)]$	$mgC\ m^{-3}$	Volume concentration of POC associated with Y in soft subclass
$[X^{prod}(z)]$	$mgX\ m^{-3}$	Volume concentration of production of X
$P_X^{prod}(z)$	$mgX\ m^{-3}\ d^{-1}$	Production of X at depth z by phytoplankton
$Z_X^{prod}(z)$	$mgX\ m^{-3}\ d^{-1}$	Production of X at depth z by zooplankton
w_X	$m\ d^{-1}$	sinking velocity of X
w_{dust}	$m\ d^{-1}$	Sinking velocity of dust
$k_x = \frac{W_X}{\lambda_X}$	d^{-1}	Remineralization rate of X
$k_Y^{hard} = \frac{W_Y}{\lambda_{hard}}$	d^{-1}	Remineralization rate of hard subclass of Y
λ_X	m	Remineralization length scale of X
λ_{hard}	m	Remineralization length scale of hard subclass
ω_X	$gC\ gY^{-1}$	POC carrying capacity of Y
f_Y^{hard}	dimensionless	Fraction of Y routed to hard subclass
$dust^{dep}$	$mgDust\ m^{-2}\ d^{-1}$	Surface dust deposition
Δz_{surf}	m	Thickness of surface grid cell
b	dimensionless	Flux attenuation parameter

Table B.4: Arrhenius function parameters
Values used in the temperature-dependency function (f_T) ($f_T = A * \text{EXP}[T_{AE}(T^{-1} - T_{ref}^{-1})]$), where A, T_{AE}, and T_{ref} are constants and T is the local temperature).

Parameter	Value	Units	Definition
A	0.5883		Normalization constant
T_{AE}	4000	K	Slope parameter
T_{ref}	294.15	K	References temperature

Table B.5: Tendency Equation - POC associated with PIC
Tendency equation for POC associated with PIC at depth z used in the ballast model. The summation of the parameter column produces the full tendency equation.

Parameter	Definition
$\omega_{PIC} f_{PIC}^{hard} \left(\frac{d[PIC^{prod}(z)]}{dt} \right)$	Tendency of hard POC associated with PIC
$\omega_{PIC} (1 - f_{PIC}^{hard}) \left(\frac{d[PIC^{prod}(z)]}{dt} \right)$	Tendency of soft POC associated with PIC
$w_{PIC} \left(\frac{d[POC_{PIC}^{hard}(z)]}{dt} \right)$	Sinking of hard POC associated with PIC
$w_{PIC} \left(\frac{d[POC_{PIC}^{soft}(z)]}{dt} \right)$	Sinking of soft POC associated with PIC
$-k_{PIC}^{hard} [POC_{PIC}^{hard}(z)]$	Remineralization of hard POC associated with PIC
$-k_{PIC} [POC_{PIC}^{soft}(z)]$	Remineralization of soft POC associated with PIC

Table B.6: Tendency Equation - POC associated with opal
Tendency equation for POC associated with opal at depth z used in the ballast model. The summation of the parameter column produces the full tendency equation.

Parameter	Definition
$\omega_{opal} f_{opal}^{hard}\left(\frac{d[opal^{prod}(z)]}{dt}\right)$	Tendency of hard POC associated with opal
$\omega_{opal}(1 - f_{opal}^{hard})\left(\frac{d[opal^{prod}(z)]}{dt}\right)$	Tendency of soft POC associated with opal
$w_{opal}\left(\frac{d[POC_{opal}^{hard}(z)]}{dt}\right)$	Sinking of hard POC associated with opal
$w_{opal}\left(\frac{d[POC_{opal}^{soft}(z)]}{dt}\right)$	Sinking of soft POC associated with opal
$-k_{opal}^{hard}[POC_{opal}^{hard}(z)]$	Remineraliation of hard POC associated with opal
$-k_{opal}[POC_{opal}^{soft}(z)]$	Remineralization of soft POC associated with opal

Table B.7: Tendency Equation - POC associated with dust
Tendency equation for POC associated with dust at depth z used in the ballast model. The summation of the parameter column produces the full tendency equation.

Parameter	Definition
$\omega_{dust} f_{dust}^{hard}\left(\frac{dust^{dep}}{\Delta z_{surf}}\right)$	Tendency of hard POC associated with dust
$\omega_{dust}(1 - f_{dust}^{hard})\left(\frac{dust^{dep}}{\Delta z_{surf}}\right)$	Tendency of soft POC associated with dust
$w_{dust}\left(\frac{d[POC_{dust}^{hard}(z)]}{dt}\right)$	Sinking of hard POC associated with dust
$w_{dust}\left(\frac{d[POC_{dust}^{soft}(z)]}{dt}\right)$	Sinking of soft POC associated with dust
$-k_{dust}^{hard}[POC_{dust}^{hard}(z)]$	Remineraliation of hard POC associated with dust
$-k_{dust}[POC_{dust}^{soft}(z)]$	Remineralization of soft POC associated with dust

Table B.8: Tendency Equation - labile POC

Tendency equation for labile POC at depth z $\left(\frac{d[POC(z)]}{dt}\right)$ used in the ballast model. The summation of the parameter column produces the full tendency equation.

Parameter	Definition
$\left(\frac{d[POC^{prod}(z)]}{dt}\right))$	Tendency of POC production by phytoplankton and zoo-plankton
$-\omega_{PIC}\left(\frac{d[PIC^{prod}(z)]}{dt}\right))$	Tendency of POC associated with PIC production
$-\omega_{opal}\left(\frac{d[opal^{prod}(z)]}{dt}\right))$	Tendency of POC associated with opal production
$-\omega_{dust}\left(\frac{dust^{dep}}{\Delta z_{surf}}\right)$	Tendency of POC associated with dust deposition
$w_{POC}\left(\frac{d[POC(z)]}{dt}\right))$	Sinking of labile POC
$-f_T k_{POC}[POC(z)]$	Remineralization of labile POC

Table B.9: ΔpCO_2 **using Kwon et al. [2009] models**

ΔpCO_2 associated with minimum and maximum b value using nutrient restoring (NR) and constant export (CE) models with rain ratio ($r = PIC/POC$) of 0 and 0.08 from Kwon et al. [2009]. The range of b was calculated using observations in the twilight and midnight zone (Twi + Mid) and just observations in the midnight zone (Mid).

	NR $r = 0.08$	NR $r = 0$	CE $r = 0.08$	CE $r = 0$
min/max b	min/max ΔpCO_2* 'base' model	min/max ΔpCO_2†	min/max ΔpCO_2‡	min/max ΔpCO_2§
Twi+Mid	0.68/1.13	-17/+27	-9/+12	-44/+68	-34/+57
Mid	0.70/0.98	-16/+12	-8/+6	-39/+33	-31/+27

*Referenced to $pCO_2(b{=}0.858) = 267$ppm
†Referenced to $pCO_2(b{=}0.858) = 240$ppm
‡Referenced to $pCO_2(b{=}0.858) = 249$ppm
§Referenced to $pCO_2(b{=}0.858) = 221$ppm

Bibliography

Armstrong, Robert et al. (2002). "A new, mechanistic model for organic carbon fluxes in the ocean based on the quantitative association of POC with ballast minerals". In: *Deep Sea Res Part Ii Top Stud Oceanogr* 49.1-3, pp. 219–236. ISSN: 0967-0645. DOI: 10.1016/S0967-0645(01)00101-1.

Arnarson, Thorarinn S and Richard G Keil (2005). "Influence of organic-mineral aggregates on microbial degradation of the dinoflagellate Scrippsiella trochoidea". In: *Geochimica et Cosmochimica Acta* 69.8, pp. 2111–2117.

Banse, Karl (1990). "New views on the degradation and disposition of organic particles as collected by sediment traps in the open sea". In: *Deep Sea Res Part Oceanogr Res Pap* 37.7, pp. 1177–1195. ISSN: 0198-0149. DOI: 10.1016/0198-0149(90)90058-4.

Barange, Manuel et al. (2017). "The cost of reducing the North Atlantic Ocean biological carbon pump". In: *Frontiers in Marine Science* 3, p. 00290.

Behrenfeld, Michael J and Paul G Falkowski (1997). "Photosynthetic rates derived from satellite-based chlorophyll concentration". In: *Limnology and oceanography* 42.1, pp. 1–20.

Berelson, William (2001). "Particle settling rates increase with depth in the ocean". In: *Deep Sea Res Part Ii Top Stud Oceanogr* 49.1-3, pp. 237–251. ISSN: 0967-0645. DOI: 10.1016/S0967-0645(01)00102-3.

Betzer, Peter R et al. (1984). "Primary productivity and particle fluxes on a transect of the equator at 153 W in the Pacific Ocean". In: *Deep Sea Research Part A. Oceanographic Research Papers* 31.1, pp. 1–11.

Bopp, Laurent et al. (2013). "Multiple stressors of ocean ecosystems in the 21st century: projections with CMIP5 models". In: *Biogeosciences* 10, pp. 6225–6245.

Boyd, P.W. and T.W. Trull (2007). "Understanding the export of biogenic particles in oceanic waters: Is there consensus?" In: *Prog Oceanogr* 72.4, pp. 276–312. ISSN: 0079-6611. DOI: 10.1016/j.pocean.2006.10.007.

Boyer, Timothy P et al. (2013). "NOAA Atlas NESDIS 72". In:

Broecker, WS and TH Peng (1982). "Tracers in the Sea, Eldigio". In: *Lamont-Doherty Geol. Obs. Columbia Univ., Palisades, NY*.

Buchanan, Pearse J et al. (2016). "The simulated climate of the Last Glacial Maximum and insights into the global marine carbon cycle". In: *Climate of the Past* 12.12, p. 2271.

Buesseler, Ken (1998). "The decoupling of production and particulate export in the surface ocean". In: *Global Biogeochem Cy* 12.2, pp. 297–310. ISSN: 1944-9224. DOI: 10.1029/97GB03366.

Buesseler, Ken O and Philip W Boyd (2009). "Shedding light on processes that control particle export and flux attenuation in the twilight zone of the open ocean". In: *Limnology and Oceanography* 54.4, pp. 1210–1232.

Buitenhuis, Erik T, Taketo Hashioka, and Corinne Le Quéré (2013). "Combined constraints on global ocean primary production using observations and models". In: *Global Biogeochemical Cycles* 27.3, pp. 847–858.

Burd, Adrian and George Jackson (2009). "Particle Aggregation". In: *Annu Rev Mar Sci* 1.1, pp. 65–90. ISSN: 1941-1405. DOI: 10.1146/annurev.marine.010908.163904.

Burd, Adrian et al. (2016). *Towards a transformative understanding of the oceanâĂŹs biological pump: Priorities for future research-Report on the NSF Biology of the Biological Pump Workshop*.

Burd, Adrian B et al. (2002). "Shining a light on the ocean's twilight zone". In: *Eos, Transactions American Geophysical Union* 83.49, pp. 573–580.

Cavan, EL et al. (2015). "Attenuation of particulate organic carbon flux in the Scotia Sea, Southern Ocean, is controlled by zooplankton fecal pellets". In: *Geophysical Research Letters* 42.3, pp. 821–830.

Cavan, Emma L et al. (2017). "Role of zooplankton in determining the efficiency of the biological carbon pump". In: *Biogeosciences* 14.1, pp. 177–186.

Ciais P, et al. (2014). *Climate change 2013: the physical science basis: Working Group I contribution to the Fifth assessment report of the Intergovernmental Panel on Climate Change*. Cambridge University Press.

De La Rocha, Christina and Uta Passow (2007). "Factors influencing the sinking of POC and the efficiency of the biological carbon pump". In: *Deep Sea Res Part Ii Top Stud Oceanogr* 54.5-7, pp. 639–658. ISSN: 0967-0645. DOI: 10.1016/j.dsr2.2007.01.004.

De La Rocha, Christina L, Nicolas Nowald, and Uta Passow (2008). "Interactions between diatom aggregates, minerals, particulate organic carbon, and dissolved organic matter: Further implications for the ballast hypothesis". In: *Global Biogeochemical Cycles* 22.4.

De La Rocha, CL (2006). "The biological pump,ÂăIn: Elderfield, H. (Ed.), The oceans and marine geochemistry". In: *The oceans and marine geochemistry* 6, p. 83.

Deuser, WG, EH Ross, and RF Anderson (1981). "Seasonality in the supply of sediment to the deep Sargasso Sea and implications for the rapid transfer of matter to the deep ocean". In: *Deep Sea Research Part A. Oceanographic Research Papers* 28.5, pp. 495–505.

Devol, Allan H and Hilairy E Hartnett (2001). "Role of the oxygen-deficient zone in transfer of organic carbon to the deep ocean". In: *Limnology and Oceanography* 46.7, pp. 1684–1690.

DeVries, Tim and Thomas Weber (2017a). "The export and fate of organic matter in the ocean: New constraints from combining satellite and oceanographic tracer observations". In: *Global Biogeochemical Cycles* 31.3, pp. 535–555.

— (2017b). "The export and fate of organic matter in the ocean: New constraints from combining satellite and oceanographic tracer observations". In: *Global Biogeochemical Cycles* 31.3, pp. 535–555.

DeVries, Tim, Francois Primeau, and Curtis Deutsch (2012). "The sequestration efficiency of the biological pump". In: *Geophys Res Lett* 39.13, n/a–n/a. ISSN: 1944-8007. DOI: 10.1029/2012GL051963.

Dunne, John et al. (2013). "GFDLâĂŹs ESM2 Global Coupled ClimateâĂŞCarbon Earth System Models. Part II: Carbon System Formulation and Baseline Simulation Characteristics*". In: *J Climate* 26.7, pp. 2247–2267. ISSN: 0894-8755. DOI: 10.1175/JCLI-D-12-00150.1.

Dutkiewicz, S., M. Follows, and P. Parekh (2005). "Interactions of the iron and phosphorus cycles: A threeâĂŘdimensional model study". In: *Global Biogeochem Cy* 19.1. ISSN: 1944-9224. DOI: 10.1029/2004GB002342.

Engel, Anja et al. (2009). "Investigating the effect of ballasting by CaCO 3 in Emiliania huxleyi: I. Formation, settling velocities and physical properties of aggregates". In: *Deep Sea Research Part II: Topical Studies in Oceanography* 56.18, pp. 1396–1407.

Eppley, Richard W and Bruce J Peterson (1979). "Particulate organic matter flux and planktonic new production in the deep ocean". In: *Nature* 282.5740, pp. 677–680.

Francois, Roger et al. (2002). "Factors controlling the flux of organic carbon to the bathypelagic zone of the ocean". In: *Global Biogeochem Cy* 16.4, pp. 34–1–34–20. ISSN: 1944-9224. DOI: 10.1029/2001GB001722.

Friedrichs, Marjorie et al. (2009). "Assessing the uncertainties of model estimates of primary productivity in the tropical Pacific Ocean". In: *J Marine Syst* 76.1-2, pp. 113–133. ISSN: 0924-7963. DOI: 10.1016/j.jmarsys.2008.05.010.

Frouin R., et al. (2002). "The SeaWiFS PAR product. ,In: Algorithm updates for the fourth SeaWiFS data reprocessing". In:

Giering, Sarah LC et al. (2014). "Reconciliation of the carbon budget in the ocean/'s twilight zone". In: *Nature* 507.7493, pp. 480–483.

Giering, Sarah LC et al. (2016). "Particle flux in the oceans: Challenging the steady state assumption". In: *Global Biogeochemical Cycles*.

Guidi, Lionel et al. (2009). "Effects of phytoplankton community on production, size, and export of large aggregates: A world-ocean analysis". In: *Limnology and Oceanography* 54.6, pp. 1951–1963.

Guidi, Lionel et al. (2015). "A new look at ocean carbon remineralization for estimating deepwater sequestration". In: *Global Biogeochem Cy* 29.7, pp. 1044–1059. ISSN: 1944-9224. DOI: 10.1002/2014GB005063.

Guidi, Lionel et al. (2016). "Plankton networks driving carbon export in the oligotrophic ocean". In: *Nature* 532.7600, pp. 465–470. ISSN: 0028-0836. DOI: 10.1038/nature16942.

Hauck, J. et al. (2015). "On the Southern Ocean CO2 uptake and the role of the biological carbon pump in the 21st century". In: *Global Biogeochem Cy* 29.9, pp. 1451–1470. ISSN: 1944-9224. DOI: 10.1002/2015GB005140.

Henson, Stephanie et al. (2011). "A reduced estimate of the strength of the ocean's biological carbon pump". In: *Geophys Res Lett* 38.4, n/a–n/a. ISSN: 1944-8007. DOI: 10.1029/2011GL046735.

Henson, Stephanie, Richard Sanders, and Esben Madsen (2012). "Global patterns in efficiency of particulate organic carbon export and transfer to the deep ocean". In: *Global Biogeochem Cy* 26.1, n/a–n/a. ISSN: 1944-9224. DOI: 10.1029/2011GB004099.

Hofmann, EE et al. (2008). "Eastern US continental shelf carbon budget integrating models, data assimilation, and analysis". In:

Honjo, Susumu et al. (2008). "Particulate organic carbon fluxes to the ocean interior and factors controlling the biological pump: A synthesis of global sediment trap programs since 1983". In: *Progress in Oceanography* 76.3, pp. 217–285.

Howard, M. et al. (2006). "Sensitivity of ocean carbon tracer distributions to particulate organic flux parameterizations". In: *Global Biogeochem Cy* 20.3, n/a–n/a. ISSN: 1944-9224. DOI: 10.1029/2005GB002499.

Ingalls, Anitra E, Zhanfei Liu, and Cindy Lee (2006). "Seasonal trends in the pigment and amino acid compositions of sinking particles in biogenic CaCO 3 and SiO 2 dominated regions of the Pacific sector of the Southern Ocean along 170 W". In: *Deep Sea Research Part I: Oceanographic Research Papers* 53.5, pp. 836–859.

Iversen, MH and Helle Ploug (2010). "Ballast minerals and the sinking carbon flux in the ocean: carbon-specific respiration rates and sinking velocity of marine snow aggregates". In: *Biogeosciences* 7.9, pp. 2613–2624.

Iversen, Morten H and Maya L Robert (2015). "Ballasting effects of smectite on aggregate formation and export from a natural plankton community". In: *Marine Chemistry* 175, pp. 18–27.

Jiao, Nianzhi et al. (2010). "Microbial production of recalcitrant dissolved organic matter: long-term carbon storage in the global ocean". In: *Nat Rev Microbiol* 8.8, pp. 593–599. ISSN: 1740-1526. DOI: 10.1038/nrmicro2386.

Jokulsdottir, Tinna and David Archer (2016). "A stochastic, Lagrangian model of sinking biogenic aggregates in the ocean (SLAMS 1.0): model formulation, validation and sensitivity". In: *Geoscientific Model Development* 9.4, pp. 1455–1476.

Jolliff, Jason et al. (2009). "Summary diagrams for coupled hydrodynamic-ecosystem model skill assessment". In: *J Marine Syst* 76.1-2, pp. 64–82. ISSN: 0924-7963. DOI: 10.1016/j.jmarsys.2008.05.014.

Kalnay, Eugenia et al. (1996). "The NCEP/NCAR 40-year reanalysis project". In: *Bulletin of the American meteorological Society* 77.3, pp. 437–471.

Keil, Richard G, Jacquelyn A Neibauer, and Allan H Devol (2016). "A multiproxy approach to understanding the" enhanced" flux of organic matter through the oxygen-deficient waters of the Arabian Sea". In: *Biogeosciences* 13.7, p. 2077.

Key, R. et al. (2004). "A global ocean carbon climatology: Results from Global Data Analysis Project (GLODAP)". In: *Global Biogeochem Cy* 18.4, n/a–n/a. ISSN: 1944-9224. DOI: 10.1029/2004GB002247.

Klaas, Christine and David Archer (2002). "Association of sinking organic matter with various types of mineral ballast in the deep sea: Implications for the rain ratio". In: *Global Biogeochem Cy* 16.4, pp. 63–1–63–14. ISSN: 1944-9224. DOI: 10.1029/2001GB001765.

Krumhardt, Kristen M et al. (2016). "Avoidable impacts of ocean warming on marine primary production: Insights from the CESM ensembles". In: *Global Biogeochemical Cycles*.

Kwon, Eun, François Primeau, and Jorge Sarmiento (2009). "The impact of reminer-alization depth on the airâĂŞsea carbon balance". In: *Nat Geosci* 2.9, pp. 630–635. ISSN: 1752-0894. DOI: `10.1038/ngeo612`.

Kwon, Eun et al. (2011). "The control of atmospheric pCO2 by ocean ventilation change: The effect of the oceanic storage of biogenic carbon". In: *Global Biogeochem Cy* 25.3, n/a–n/a. ISSN: 1944-9224. DOI: `10.1029/2011GB004059`.

Lam, Phoebe J, Scott C Doney, and James KB Bishop (2011). "The dynamic ocean biological pump: Insights from a global compilation of particulate organic carbon, CaCO3, and opal concentration profiles from the mesopelagic". In: *Global Biogeochemical Cycles* 25.3.

Large, William G, James C McWilliams, and Scott C Doney (1994). "Oceanic vertical mixing: A review and a model with a nonlocal boundary layer parameterization". In: *Reviews of Geophysics* 32.4, pp. 363–403.

Laufkötter, C. et al. (2015). "Drivers and uncertainties of future global marine primary production in marine ecosystem models". In: *Biogeosciences* 12.23, pp. 6955–6984. ISSN: 1726-4170. DOI: `10.5194/bg-12-6955-2015`.

Laws, Edward A et al. (2000). "Temperature effects on export production in the open ocean". In: *Global Biogeochemical Cycles* 14.4, pp. 1231–1246.

Lazzari, P et al. (2012). "Seasonal and inter-annual variability of plankton chlorophyll and primary production in the Mediterranean Sea: a modelling approach." In: *Biogeosciences Discussions* 8.3.

Le Moigne, Frederic AC et al. (2013). "Enhanced rates of particulate organic matter remineralization by microzooplankton are diminished by added ballast minerals". In: *Biogeosciences* 10.9, p. 5755.

Le Quéré, Corinne et al. (2016). "Global carbon budget 2016". In: *Earth System Science Data* 8.2, p. 605.

Lebrato, Mario et al. (2012). "Jelly-falls historic and recent observations: a review to drive future research directions". In: *Hydrobiologia* 690.1, pp. 227–245.

Lee, Younjoo J et al. (2015). "An assessment of phytoplankton primary productivity in the Arctic Ocean from satellite ocean color/in situ chlorophyll-a based models". In: *Journal of Geophysical Research: Oceans* 120.9, pp. 6508–6541.

Lima, I., P. Lam, and S. Doney (2014). "Dynamics of particulate organic carbon flux in a global ocean model". In: *Biogeosciences* 11.4, pp. 1177–1198. ISSN: 1726-4170. DOI: `10.5194/bg-11-1177-2014`.

Longhurst, A.R. (2006). "Ecological Geography of the Sea. 2nd Edition." In: *Academic Press, San Diego, 560p*.

Lutz, Michael, Robert Dunbar, and Ken Caldeira (2002). "Regional variability in the vertical flux of particulate organic carbon in the ocean interior". In: *Global Biogeochem Cy* 16.3, pp. 11–1–11–18. ISSN: 1944-9224. DOI: `10.1029/2000GB001383`.

Lutz, Michael et al. (2007). "Seasonal rhythms of net primary production and particulate organic carbon flux to depth describe the efficiency of biological pump

in the global ocean". In: *J Geophys Res Oceans 1978 2012* 112.C10. ISSN: 2156-2202. DOI: 10.1029/2006JC003706.

Mahowald, Natalie et al. (2005). "Atmospheric global dust cycle and iron inputs to the ocean". In: *Global Biogeochem Cy* 19.4, n/a–n/a. ISSN: 1944-9224. DOI: 10.1029/2004GB002402.

Mari, Xavier et al. (2017). "Transparent exopolymer particles: Effects on carbon cycling in the ocean". In: *Progress in Oceanography* 151, pp. 13–37.

Marinov, I. et al. (2008a). "How does ocean biology affect atmospheric pCO2? Theory and models". In: *J Geophys Res Oceans 1978 2012* 113.C7. ISSN: 2156-2202. DOI: 10.1029/2007JC004598.

Marinov, I. et al. (2008b). "Impact of oceanic circulation on biological carbon storage in the ocean and atmospheric pCO2". In: *Global Biogeochem Cy* 22.3, n/a–n/a. ISSN: 1944-9224. DOI: 10.1029/2007GB002958.

Marsay, Chris M et al. (2015). "Attenuation of sinking particulate organic carbon flux through the mesopelagic ocean". In: *Proceedings of the National Academy of Sciences* 112.4, pp. 1089–1094.

Marshall, John et al. (1997a). "A finite-volume, incompressible Navier Stokes model for studies of the ocean on parallel computers". In: *Journal of Geophysical Research: Oceans* 102.C3, pp. 5753–5766.

Marshall, John et al. (1997b). "Hydrostatic, quasi-hydrostatic, and nonhydrostatic ocean modeling". In: *Journal of Geophysical Research: Oceans* 102.C3, pp. 5733–5752.

Martin, John H et al. (1987). "VERTEX: carbon cycling in the northeast Pacific". In: *Deep Sea Research Part A. Oceanographic Research Papers* 34.2, pp. 267–285.

Mayer, Lawrence (1994). "Surface area control of organic carbon accumulation in continental shelf sediments". In: *Geochim Cosmochim Ac* 58.4, pp. 1271–1284. ISSN: 0016-7037. DOI: 10.1016/0016-7037(94)90381-6.

Moore, J., Scott Doney, and Keith Lindsay (2004). "Upper ocean ecosystem dynamics and iron cycling in a global threeâĂŘdimensional model". In: *Global Biogeochem Cy* 18.4, n/a–n/a. ISSN: 1944-9224. DOI: 10.1029/2004GB002220.

Mouw, Colleen B et al. (2016a). "Global ocean particulate organic carbon flux merged with satellite parameters". In: *Earth System Science Data* 8.2, p. 531.

— (2016b). "Phytoplankton size impact on export flux in the global ocean". In: *Global Biogeochemical Cycles* 30.10, pp. 1542–1562.

Nash, J Eamonn and Jonh V Sutcliffe (1970). "River flow forecasting through conceptual models part IâĂŤA discussion of principles". In: *Journal of hydrology* 10.3, pp. 282–290.

Pabortsava, Katsiaryna et al. (2017). "Carbon sequestration in the deep Atlantic enhanced by Saharan dust". In: *Nature Geoscience* 10.3, pp. 189–194.

Pace, Michael L et al. (1987). "Primary production, new production and vertical flux in the eastern Pacific Ocean". In: *Nature* 325.6107, pp. 803–804.

Pairaud, IL et al. (2011). "Hydrology and circulation in a coastal area off Marseille: Validation of a nested 3D model with observations". In: *Journal of Marine Systems* 88.1, pp. 20–33.

Parekh, P et al. (2006). "Atmospheric carbon dioxide in a less dusty world". In: *Geophysical research letters* 33.3.

Passow, Uta (2004). "Switching perspectives: Do mineral fluxes determine particulate organic carbon fluxes or vice versa?" In: *Geochem Geophys Geosystems* 5.4, n/a–n/a. ISSN: 1525-2027. DOI: `10.1029/2003GC000670`.

Passow, Uta and Craig A Carlson (2012). "The biological pump in a high CO2 world". In: *Marine Ecology Progress Series* 470, pp. 249–271.

Passow, Uta and Christina De La Rocha (2006). "Accumulation of mineral ballast on organic aggregates". In: *Global Biogeochem Cy* 20.1, n/a–n/a. ISSN: 1944-9224. DOI: `10.1029/2005GB002579`.

Ploug, Helle et al. (2008). "Production, oxygen respiration rates, and sinking velocity of copepod fecal pellets: direct measurements of ballasting by opal and calcite". In: *Limnol. Oceanogr. 53 (2)*, pp. 469–476.

Pomeroy, Lawrence R and Don Deibel (1986). "Temperature regulation of bacterial activity during the spring bloom in newfoundland coastal waters." In: *Science(Washington)* 233.4761, pp. 359–361.

Pomeroy, LR and WJ Wiebe (1991). "Bacterial responses to temperature and substrate concentration during the Newfoundland spring bloom." In: *Marine ecology progress series. Oldendorf* 75.2, pp. 143–159.

Primeau, François (2005). "Characterizing transport between the surface mixed layer and the ocean interior with a forward and adjoint global ocean transport model". In: *Journal of Physical Oceanography* 35.4, pp. 545–564.

Ragueneau, Olivier et al. (2000). "A review of the Si cycle in the modern ocean: recent progress and missing gaps in the application of biogenic opal as a paleo-productivity proxy". In: *Global and Planetary Change* 26.4, pp. 317–365.

Saba, V. et al. (2011). "An evaluation of ocean color model estimates of marine primary productivity in coastal and pelagic regions across the globe". In: *Biogeosciences* 8.2, pp. 489–503. ISSN: 1726-4170. DOI: `10.5194/bg-8-489-2011`.

Saba, Vincent et al. (2010). "Challenges of modeling depthâĂŘintegrated marine primary productivity over multiple decades: A case study at BATS and HOT". In: *Global Biogeochem Cy* 24.3, n/a–n/a. ISSN: 1944-9224. DOI: `10.1029/2009GB003655`.

Sanders, Richard J et al. (2016). "Controls over Ocean Mesopelagic Interior Carbon Storage (COMICS): Fieldwork, Synthesis, and Modeling Efforts". In: *Frontiers in Marine Science* 3, p. 136.

Sarmiento, J.L. and N. Gruber (2006). *Ocean Biogeochemical Dynamics*. Princeton, NJ.: Princeton University Press.

Schlitzer, Reiner (2000). "Applying the adjoint method for biogeochemical modeling: export of participate organic matter in the world ocean". In: *Inverse methods in global biogeochemical cycles*, pp. 107–124.

Schlitzer, Reiner (2002). "Carbon export fluxes in the Southern Ocean: results from inverse modeling and comparison with satellite-based estimates". In: *Deep Sea Research Part II: Topical Studies in Oceanography* 49.9, pp. 1623–1644.

Siegel, David et al. (2016). "Prediction of the Export and Fate of Global Ocean Net Primary Production: The EXPORTS Science Plan". In: *Front Mar Sci* 3. DOI: `10.3389/fmars.2016.00022`.

Sigman, Daniel M and Edward A Boyle (2000). "Glacial/interglacial variations in atmospheric carbon dioxide". In: *Nature* 407.6806, pp. 859–869.

Smith Jr, KL et al. (2014). "Large salp bloom export from the upper ocean and benthic community response in the abyssal northeast Pacific: day to week resolution". In: *Limnology and Oceanography* 59.3, pp. 745–757.

Steinberg, Deborah et al. (2008). "Bacterial vs. zooplankton control of sinking particle flux in the ocean's twilight zone". In: *Limnol Oceanogr* 53.4, pp. 1327–1338. ISSN: 1939-5590. DOI: `10.4319/lo.2008.53.4.1327`.

Steinberg, Deborah K and Michael R Landry (2017). "Zooplankton and the Ocean Carbon Cycle". In: *Annual Review of Marine Science* 9, pp. 413–444.

Stow, Craig et al. (2009). "Skill assessment for coupled biological/physical models of marine systems". In: *J Marine Syst* 76.1-2, pp. 4–15. ISSN: 0924-7963. DOI: `10.1016/j.jmarsys.2008.03.011`.

Suess, Erwin (1980). "Particulate organic carbon flux in the oceansâĂŤsurface". In: *Nature* 288, p. 261.

Taylor, Karl (2001). "Summarizing multiple aspects of model performance in a single diagram". In: *J Geophys Res Atmospheres 1984 2012* 106.D7, pp. 7183–7192. ISSN: 2156-2202. DOI: `10.1029/2000JD900719`.

Van Mooy, Benjamin AS, Richard G Keil, and Allan H Devol (2002). "Impact of suboxia on sinking particulate organic carbon: Enhanced carbon flux and preferential degradation of amino acids via denitrification". In: *Geochimica et Cosmochimica Acta* 66.3, pp. 457–465.

Villa-Alfageme, M. et al. (2016). "Observations and modeling of slowâĂŘsinking particles in the twilight zone". In: *Global Biogeochem Cy* 28.11, pp. 1327–1342. ISSN: 1944-9224. DOI: `10.1002/2014GB004981`.

VLIZ (2009). "Longhurst biogeographical provinces". In: URL: `[Availableathttp://www.marineregions.org/.]`.

Volk, Tyler and Martin I Hoffert (1985). "Ocean carbon pumps: Analysis of relative strengths and efficiencies in ocean-driven atmospheric CO2 changes". In: *The Carbon Cycle and Atmospheric CO: Natural Variations Archean to Present*, pp. 99–110.

Walsh, Ian, Jack Dymond, and Robert Collier (1988). "Rates of recycling of biogenic components of settling particles in the ocean derived from sediment trap experiments". In: *Deep Sea Research Part A. Oceanographic Research Papers* 35.1, pp. 43–58.

Williams, Richard G and Michael J Follows (2011). *Ocean dynamics and the carbon cycle: Principles and mechanisms*. Cambridge University Press.

Wilson, JD, S Barker, and A Ridgwell (2012). "Assessment of the spatial variability in particulate organic matter and mineral sinking fluxes in the ocean interior: Implications for the ballast hypothesis". In: *Global Biogeochemical Cycles* 26.4.

Yool, A., E. Popova, and T. Anderson (2010). "MEDUSA: a new intermediate complexity plankton ecosystem model for the global domain". In: *Geoscientific Model Dev Discuss* 3.4, pp. 1939–2019. ISSN: 1991-9611. DOI: `10.5194/gmdd-3-1939-2010`.

Yu, J et al. (2016). "Sequestration of carbon in the deep Atlantic during the last glaciation". In: *Nature Geoscience.*